Heterogeneous Fenton-like catalytic degradation of phenazine dye over CeO_2 (CP-2) nanoscale powder

E. Abdelkader[1]*

[1]Université des Sciences et de la Technologie d'Oran Mohammed Boudiaf, Laboratoire des Sciences, Technologie et Génie des Procédés, BP 1505 El M'naouar 31000 Oran, Algérie

Abstract

A heterogeneous Fenton-like process was explored for oxidation of phenazine dye using ceria polishing material (CP-2). XRD, SEM, FTIR, UV-vis DRS, and pH_{PZC} techniques were applied to characterize the catalyst features. The performance of the heterogeneous Fenton-like process was investigated under various parameters (reaction time, pH, H_2O_2 concentration, catalyst dosage, initial dye concentration, temperature of the medium, and inorganic salt content). Results indicated that the main content of CP-2 catalyst was CeO_2 (60-70%) with lower contents of La_2O_3 (30-40%), Pr_6O_{11} (≤6%), Nd_2O_3, and CaF_2 (≤5%). CP-2 possessed a typical CeO_2 cubic fluorite structure with high content of rare earth oxides (REO) and α-Fe_2O_3. The average crystallite size and band gap energy of CP-2 were found to be 37.2 nm and 3.0 eV, respectively. Over 81.3% of neutral red (NR) oxidation efficiency was achieved in 60 min. Pseudo-first-order kinetic model gave the best fit with an acceptable coefficient of determination R^2. The activation energy (E_a) was 16.4 kJ/mol suggesting that the degradation reaction proceeded with a low energy barrier and the removal process was feasible, spontaneous, and endothermic. The synergistic effect of Fe- and/or REO-CP-2 and H_2O_2 greatly enhanced the reactive oxygen species (ROS) such as $^{\bullet}OH$, $O_2^{\bullet-}$, $^1O_2$, and $HO_2^{\bullet}$ for effective oxidation of NR via a heterogeneous Fenton-like process.

Keywords: ceria, hydrogen peroxide, phenazine dye, heterogeneous Fenton-like process, kinetics.

INTRODUCTION

Wastewaters from the textile, dyeing, leather, pharmaceutical, paper, cosmetic, plastic, and synthetic detergent industries are mainly refractory, non-biodegradable, environmentally toxic and harmful to the human health, and have potential bioaccumulation and persistence in sediments of their degradation/biotransformation by-products [1, 2]. Thus, wastewater treatment, refinement, and recycling are crucial for environmental pollution control and industrial applications [2, 3]. Recently, innovative approaches, such as advanced oxidation processes (AOPs) based on the *in situ* generation of highly reactive hydroxyl radicals ($^{\bullet}OH$) have been recommended as the most effective technique for water and wastewater treatment owing to the enhanced biodegradability, extensive ability of recalcitrance substances degradation and mineralization as well as efficient toxicity reduction [4-9]. It is recognized that the conventional AOPs (O_3, O_3/UV, O_3/H_2O_2, O_3/H_2O_2/UV, O_3/catalysts, UV/H_2O_2, Fe^{2+}/H_2O_2, Fe^{3+}/H_2O_2, and Fe^{2+}/H_2O_2/UV) or with non-conventional AOPs (photo-electro-Fenton and sono-electro-Fenton processes) techniques are detrimental for effective treatment of wastewater [10-13]. Among these technologies, the homogeneous Fenton process (Fe^{2+}/H_2O_2 and Fe^{3+}/H_2O_2) is one of the most investigated strategies that has been applied extensively for the abatement of a large number of hazardous and recalcitrant organic pollutants, especially many non-biodegradable substances in an aqueous phase, sediment, and soil. Furthermore, the Fenton process can be employed in full-size wastewater treatment including landfill leachate and dye process wastewater due to its non-selectivity towards organic compounds [14]. The main oxidation mechanism in the homogeneous Fenton process, where ferrous ions (Fe^{2+}) unceasingly react with hydrogen peroxide (H_2O_2) to generate hydroxyl radicals ($^{\bullet}OH$) with a strong oxidizing ability (Eq. A). The synchronized reduction of ferric ions (Fe^{3+}) to ferrous ions Fe^{2+} realizes the circulation of iron ions. Nevertheless, Eq. B is the rate-determining step, whose rate is nearly 1/6000 that of Eq. A, which greatly declines the effectiveness of Fe^{3+}/Fe^{2+} circulation [15]. The inhibition of Fe^{3+}/Fe^{2+} circulation induces not only the deficient utilization efficiency of H_2O_2 but also the aggregation of Fe^{3+}. It precipitates to form ferric hydroxide [$Fe(OH)_3$], namely iron sludge, when the pH value is higher than 3, leading to thorny secondary pollution [16].

$$Fe^{2+} + H_2O_2 + H^+ \rightarrow Fe^{3+} + {}^{\bullet}OH + H_2O \quad (A)$$

$$Fe^{3+} + H_2O_2 \rightarrow Fe^{2+} + HO_2^{\bullet} + H^+ \quad (B)$$

Nevertheless, this Fenton process still possesses some drawbacks such as restricted pH range (always around 2-3), the low utilization efficiency of H_2O_2, iron deactivation by the formation of complexing reagents such as phosphate ions, huge amount of iron sludge originating from the process, and requirement of high technology and operation cost.

**abdelkader.elaziouti@univ-usto.dz*

https://orcid.org/0000-0002-0078-4816

Thus, to overwhelm these disadvantages, heterogeneous Fenton and heterogeneous Fenton-like processes have recently been attracting a great deal of interest owing to their unique ability to resolve the aforementioned concerns related to the homogeneous Fenton process [17]. The general requirements for heterogeneous Fenton catalysts are effectiveness at widespread ranges of pH (5-7), high efficiency related to contaminant removal rates and H_2O_2 utilization, stability of iron within the catalyst structure in heterogeneous catalysis over long periods of application, generation of little iron sludge, leaching of low iron ions from the solid catalyst into solution after carrying out the degradation process, low cost, abundant resources, and harmlessness. Many studies focused on the development of iron-derived heterogeneous Fenton catalyst systems including Fe-ZSM-5 [18], Fe(II)/meso-Al_2O_3 [19], Fe(III) oxide/carbon [20], magnetic α-Fe_2O_3/MCM-41 [21], Fe/SBA-15 [22], Fe/TUD-1 [23], Fe/clay [24], CeO_2 nanosheets [25], CuFe/ZSM-5 [26], stabilized CuO nanoparticles [27], CuO/CeO_2 [28], Cu-functionalized titanate nanotubes [29], $CuFeO_2$ [30], Cu/MCM-41 [31], Cu/TUD-1 [32], $LiFePO_4$ microcrystals [33], Fe_3O_4 [34], $BiFeO_3$ [35], FeOCl [36], $LiFe(WO_4)_2$ [37], iron-loaded zeolite [38], iron-containing clay [39], and carbon-based materials, which are all reported to exhibit excellent degradation activity towards various organic pollutants. However, many of these heterogeneous catalysts still operate under acidic conditions only, and the generation of hydroxyl radicals is strongly affected by H_2O_2 and Fe^{3+} species, leading to a noticeable drop in degradation efficiency [40]. Recent investigations have focused on the designing of novel hetero-catalysts with larger surface area and higher responses in degradation processes. Three possible mechanisms have been proposed for an heterocatalyst action in Fenton processes: i) iron leaching to the reaction solution and activating hydrogen peroxide through a homogeneous pathway; and/or ii) decomposition of H_2O_2 to •OH radicals by binding of H_2O_2 with iron species on the surface of the catalyst and its decomposition to •OH radicals; or iii) chemisorption of probe molecule on the catalyst surface [41, 42]. Various heterogeneous catalyst systems have been used in Fenton process reactions. Amongst them, iron minerals are relatively less priced and can be separated magnetically from the reaction medium [43]. Applications of Fe-rich bentonite [44], fly ash-based catalysts [45], and molybdenum carbide doped with nanostructured nickel [46] have been reviewed in detail.

Currently, cerium oxide (CeO_2) as crucial rare-earth oxide material has attracted great interest in recent years due to its wide variety of environment and energy-related applications such as solid-state electrolytes used for electrochemical devices, three-way catalysts (TWC), sunscreens for ultraviolet absorbents, adsorption, substantial oxygen storage capacity (OSC), hybrid solar cells, H_2S removal, luminescent materials for violet/blue fluorescence, biotechnology, medicine, and polishing materials [47]. Red cerium oxide as a polishing material is an efficient abrasive for the polishing of glass. The high performance made it very popular in the glass industry. Among others, applications of CeO_2 powder are for polishing optical eyeglasses, flat glasses (wafer), mobile control panels, LCD glass, windshield glass, diamond, and crystals. These applications take benefit of cerium's high thermodynamic affinity for oxygen and sulfur. The most fascinating properties of CeO_2 are the high dielectric constant (ε=24.5), the broad band gap (around ~3.2 eV) making the material sensitive to ultraviolet light, the presence of empty 4f energy levels that facilitate the electron transfers, the high stability in the reaction medium, the high oxygen mobility related to the reversible Ce^{4+}/Ce^{3+} transformation, and the ability to form nonstoichiometric oxygen-deficient CeO_{2-x} oxide [48]. The presence of defect centers in the CeO_2 together with the high oxygen mobility and the consequential redox properties can be exploited in the heterogeneous Fenton-like reactions, even though there are few studies focused on the removal of organic pollutants from wastewater using heterogeneous Fenton-like catalysts based on CeO_2. For example, the Fe°/CeO_2 composite was synthesized and applied for the removal of chlorophenols by various processes including the Fenton reaction; the introduction of CeO_2 could facilitate the generation of chemisorbed oxygen on the surface and the dissolution of Fe° [49]. Generally, metal atoms adsorbed by CeO_2 can interact with the (111) and (110) crystal surfaces along with electron transfer; doping metal ions into the lattice of CeO_2 can improve its catalytic activity [50]. Fenton-like catalytic degradation of bisphenol F in aqueous solution by using perovskite-ceria composites (CeO_2-$LaFeO_3$ and CeO_2-$LaCuO_3$) has been reported [51]. Gao et al. [52] reported that H_2O_2 would be adsorbed on CeO_2 more easily due to the oxygen vacancies (OVs) that were beneficial for Fenton-like reaction. Zhang et al. [53] found that ceria could accelerate nanoscale zero-valent iron to assist heterogeneous Fenton oxidation of tetracycline. An efficient Fenton-like catalyst CuO/CeO_2 synthesized using ultrasonic impregnation and used to remove diclofenac from the water was reported by Zhu et al. [54]. Their work reports that the synergistic effect between CuO and CeO_2 on diclofenac removal might be caused by more OVs generation and electronic interactions between Cu and Ce species in CuO/CeO_2 [54]. Zhang et al. [55] developed ceria-Prussian blue (CeO_2-PB) composites by physical and chemical loading methods for the heterogeneous Fenton-like catalytic oxidation of norfloxacin (NOR). They showed that the PB/CeO_2 significantly enhanced the removal of NOR, which indicated a synergistic effect between PB and CeO_2, highlighting the synergetic catalysis of H_2O_2 by Fe^{3+}/Fe^{2+} and Ce^{3+}/Ce^{4+} redox couples [55].

Herein, in this study, we explore the heterogeneous Fenton-like process using CeO_2 polishing material (denoted as CP-2), as potential material for the degradation of neutral red (NR) phenazine dye, chosen as a model compound pollutant, together with H_2O_2. Firstly, CP-2 material was characterized by XRD, SEM, FTIR, UV-vis DRS, and pH_{PZC} techniques. Secondly, the impact of various operating parameters such as the pH solution, H_2O_2 concentration, material dosage, initial dye concentration, the temperature of

the medium, and inorganic salt content on the heterogeneous oxidation of NR dye by CeO_2 polishing material (CP-2) was investigated in details. Additionally, the degradation reactions were correlated with the pseudo-first-order kinetic model. Finally, to compare the NR degradation efficiency of heterogeneous Fenton-like processes using CeO_2 polishing material (CP-2) as a catalyst, three preliminary experiments were carried out under the following conditions such as CP-2 material only (adsorption process), H_2O_2 only (homogeneous oxidation process), and CP-2 material catalyst along with hydrogen peroxide, H_2O_2 (heterogeneous Fenton-like process). Commercial CeO_2 (denoted as CeO_2-com) was used for comparison. The plausible mechanism of heterogeneous Fenton-like reaction over α-Fe_2O_3/REO-CP-2/H_2O_2 system was proposed.

MATERIALS AND METHODS

Materials: commercial CeO_2 (99.99%) and hydrogen peroxide (H_2O_2 30%) were provided from Aldrich. A cerium oxide (CeO_2) powder for polishing (denoted as CP-2; White Color Powder, Hunan Haozhi Technol., China) was used. Table I displays the physical properties of the CP-2 color powder. A phenazine group cation, neutral red dye (3-amino-7-dimethylamino-2-methylphenazine hydrochloride) was provided from a commercial source. Distilled water was used for the preparation of various solutions. The characteristics of the neutral red (NR) dye used in this study are shown in Table II.

Table I - Physical properties of cerium oxide (CeO_2) powder for polishing.

Characteristic	Value	Lower	Upper
CeO_2/REO ratio (%)	75	65	No
TREO content (%)	94.54	90	No
Density, ϱ ($g.cm^{-3}$)	1.1	0.9	1.2
D_{10} (nm)	610	200	No
D_{50} (μm)	1.35	1.2	No
D_{90} (μm)	6.21	No	10
CeO_2		60-70%	
La_2O_3		30-40%	
Pr_6O_{11}		≤ 6%	
F		≤ 5%	

REO: rare earth oxides; TREO: total REO; F: fluorite (fluorspar), calcium fluoride, CaF_2.

Table II - Characteristics of neutral red (NR) dye used [56, 57].

Characteristic	Data	
CAS	553-24-2	
Color index	50040	
Chemical formula	$C_{15}H_{17}N_4Cl$	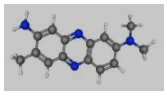
Molecular mass (g/mol)	288.78	
Melting point (°C)	290	

CAS: Chemical Abstracts Service.

Catalyst characterization: the X-ray diffraction (XRD) patterns were recorded with a diffractometer (D8 Advance, Bruker) using CuKα radiation (wavelength, λ=0.154178 nm) in the 2θ range from 10° to 80° and with a scanning rate of 10 °/min. The average crystallite size (D_{XRD}) of CP-2 material was calculated from the Scherrer equation [58]:

$$D_{XRD} = \frac{K.\lambda}{\beta \sin\theta} \quad (C)$$

where β, θ, and K are the full-width at half maximum (FWHM) of the peaks, Bragg angle, and the shape factor equal to 0.9, respectively. The specific surface area can be estimated by the BET (Brunauer, Emmett, and Teller) model, based on the adsorption of a monomolecular layer of nitrogen on the surface of the sample [59]. Since the specific surface area is intimately linked to particle size, particle size distribution determination allows, a priori, the estimation of the specific surface area of materials with other physical parameters such as material density from:

$$S_e = \frac{6}{\rho D_S} \quad (D)$$

where D_S is the mean diameter based on the surface area, also known as the Sauter diameter (μm), defined as the diameter of a sphere with the same surface area as the particle, and ϱ is the theoretical density ($g.cm^{-3}$) of the material. The estimated specific surface area (S_e) of CP-2 material was assessed by replacing D_S with the median diameter D_{50} (diameter below which 50% by volume of the total particles is found), as one of the important parameters characterizing particle size distribution in Eq. D [60]. Scanning electron microscopy (SEM) images were obtained with a microscope (S4800 FESEM, Hitachi). Fourier transform infrared (FTIR) spectrum was recorded on a spectrophotometer (Vertex70, Bruker) in the range of 4000 to 400 cm^{-1}. The optical properties of all materials were determined using a UV-vis diffuse reflectance spectrophotometer (DRS, Lambda 650, Perkin Elmer) in the wavelength range of 200-900 nm.

Catalytic test: heterogeneous Fenton-like oxidation experiments were conducted by mixing 100 mL of NR dye with 10 mg of CP-2 material (initial concentration of 10 $mg.L^{-1}$; mass/volume ratio of 0.1 $g.L^{-1}$) at room temperature and pH 2 (pH-meter, pH 210, Hanna) for 60 min in the dark to reach adsorption/desorption equilibrium. After that, an aliquot of hydrogen peroxide (H_2O_2, 1 mL, 5 mM) was added to the previous suspension to initiate the oxidation reaction. Then, aliquots were collected at given time intervals, followed by suspension separation (centrifuge, EBA, Hettich). The dye concentration in the filtrates before and after oxidation was determined using a mono-beam spectrophotometer (UV mini-1240, Shimadzu) at a maximum wavelength of 520 nm. In this study, various operating parameters such as the pH solution (2-12), H_2O_2 concentration (2.5-25 mM), CP-2 material

dosage (0.25-1.50 g.L^{-1}), initial NR dye concentration (10-60 mg.L^{-1}), the temperature of the medium (25-60 °C), and inorganic salt content (1-4 g) on the heterogeneous Fenton-like oxidation process were investigated in details. The adsorption percentage η(%) and the heterogeneous Fenton-like oxidation percentage η'(%) of CP-2 material were assessed according to:

$$\eta(\%)= \frac{C_i - C_{60}}{C_i} .100 \quad (E)$$

$$\eta'(\%)= \frac{C_{60} - C_f}{C_{60}} .100 \quad (F)$$

where C_i is the dye initial concentration (mg.L^{-1}), C_{60} is the dye residual concentration after adsorption/desorption equilibrium (mg·L^{-1}), and C_f is the dye residual concentration under oxidation conditions after certain intervals (mg.L^{-1}). Following the pseudo-first-order model, the apparent reactions rate constants of the heterogeneous Fenton-like oxidation process could be measured from the following expression:

$$C = C_0.e^{-K_{app}.t} \quad (G)$$

where $K_{app}=K_1$ is the apparent reaction rate constant, C_0 is the initial concentration of NR solution at t=0 and C is the concentration of NR solution at time t. The plot of ln(C/C_0) vs. t should give a straight line, whose slope is equal to -K_{app}.

RESULTS AND DISCUSSION

Physical and chemical properties of CP-2 polishing powder: the main content was CeO_2 (60-70%) with lower contents of La_2O_3 (30-40%), Pr_6O_{11} (≤6%), Nd_2O_3, and F (fluorite, CaF_2 ≤5%). CeO_2/REO (rare earth oxides) ratio in the CP-2 powder was 75%, while the TREO (total rare earth oxides) was found to be 94.5% and density around 1.1 g.cm^{-3} (Table I). The red color of the CP-2 polishing powder may be attributed to the presence of Pr_6O_{11}. Besides, the CP-2 material was polycrystalline in nature exhibiting three classes of the cumulative particle size distribution which gave an indication of particle size of the fine (D_{10}) and coarse (D_{90}) fractions, and of the median particle size (D_{50}). The median diameter (D_{50}) is one of the important parameters characterizing particle size distribution. It is the value of the diameter at 50% in the cumulative distribution. D_{50} was 1.35 μm, then 50% of the particles in the CP-2 material were larger than 1.35 μm. D_{10} of 0.61 μm means 10% of the CP-2 material was below 0.61 μm in size and D_{90} of 6.21 μm means that 90% of the sample had a size of 6.21 μm or smaller.

XRD analysis: Fig. 1 shows the XRD patterns of CeO_2-com and CP-2 material powders. The XRD pattern of pristine CeO_2-com showed diffraction peaks at 2θ values of 28.02°, 33.11°, 47.45°, and 56.3° that can be ascribed to (111), (200), (220), and (311) crystal planes of cubic fluorite structure of CeO_2 (space group Fm-3m) with lattice constant a=0.5418 nm (calculated from its corresponding XRD pattern data obtained by Fullprof program), which was in good agreement with the JCPDS file 34-0394 for CeO_2 [2]. The peaks were very sharp indicating well crystalline nature of the material. In the XRD pattern of CP-2 material, extra peaks were detected corresponding to (012) and (104) crystal planes positioned at 2θ values of 24.1° and 32° which can be attributed probably to hematite (α-Fe_2O_3) with rhombohedral structure (JCPDS 33-0664). Besides, in the 2θ range from 25° to 35°, there was a shift of the characteristic peaks towards lower 2θ angles and the intensity of peaks decreased, indicating the existence of Fe in the lattice of the CP-2 sample. The ionic radius of Ce^{4+} is 0.087 nm, while that for Fe^{3+} is 0.063 nm. Therefore, due to the size variation of Fe and host atom (Ce^{4+}), structural distortions occur [61]. Thus, the shifting of peaks to lower angles implies a decrease in interplanar distance. Furthermore, the CP-2 exhibited broad diffraction peaks, indicative of small scattering domain sizes. Also, the additional peak at the 2θ value of 27.8° can be assigned possibly to rare earth oxides (REO) generated by extrinsic doping of Ce^{3+} (in oxygen-deficient ceria) by Do^{3+} (La^{3+}, Pr^{3+}, Nd^{3+}) in doped ceria, in perfect agreement with the TREO content (Table I). The increase of lattice parameter in CP-2 (a=5.418 Å) compared to the pristine CeO_2 (a=0.5413 nm) can be explained in terms of the associated partial reduction of Ce^{4+} to Ce^{3+} and a substantial concentration of point defects (oxygen vacancies), which led to lattice expansion. Moreover, the average crystallite size of the CP-2 sample, calculated from the data of full-width at half-maximum (FWHM) of (111) characteristic plane using the Scherrer's formula, equals 37 nm. Table III summarizes the results of the unit cell parameter a, the average crystallite size, the theoretical density measurements, and the estimated specific surface area for CeO_2-com and CP-2 materials. The estimated specific surface area of the CP-2 sample obtained from the particle size distribution data (Table I), and another physical parameter such as material density, was found to be 4.04 m^2.g^{-1}.

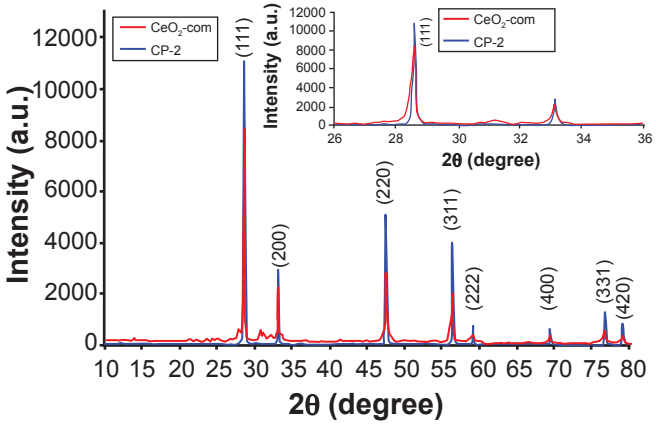

Figure 1: XRD patterns of CeO_2-com and CP-2 powders (inset: XRD patterns in the range of 26° to 36°).

FTIR analysis: the FTIR spectrum of the CP-2 material is depicted in Fig. 2. The band at 844.05 cm^{-1} can be

Table III - Crystallographic parameters of CeO_2-com and CP-2 powders.

Abbreviation	Catalyst	a (nm)	D_{XRD} (nm)	D_{50} (μm)	S_e ($m^2.g^{-1}$)	ϱ ($g.cm^{-3}$)
CeO_2	JCPDS 34-0394	0.54113	-	-	-	-
CeO_2-com	Commercial CeO_2	0.54110(2)	117	-	-	7.23
CP-2	CeO_2 polishing agent	0.5418	37.16	1.35	4.04	1.1

a: unit cell parameter; D_{XRD}: average crystallite size; D_{50}: median particle diameter; S_e: estimated specific surface area; ϱ: density.

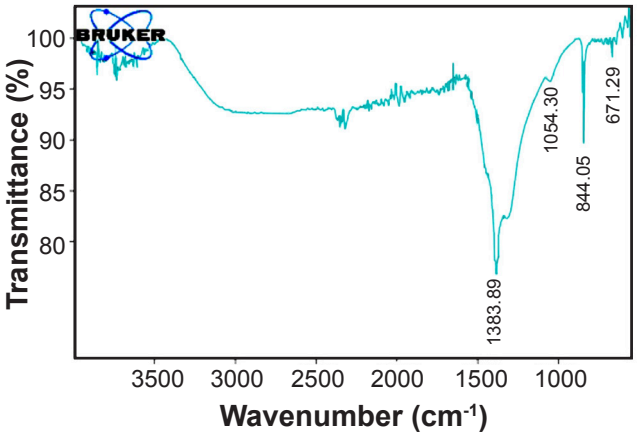

Figure 2: FTIR spectrum of CP-2 material.

attributed to the (Ce-O) stretching vibration mode. The observed bands at 671.29, 1054.30, and 1383.89 cm^{-1} can be ascribed to the (Ce-O-Ce) stretching vibration mode [62]. The broad absorption band at 3300 cm^{-1} can be regarded as the stretching mode of H_2O of the free or absorbed water molecules on the surface of the CP-2 material.

SEM analysis: the morphological features of the CP-2 material were observed by SEM (Fig. 3). According to the high-resolution SEM image (Fig. 3a), CP-2 material showed a randomly and irregularly shaped cluster of variable nanoparticles whose average diameter was in the range of 715 nm-4.52 μm. The surface energy is shown to be crucial with respect to the thermodynamic barrier to the formation of particles. The accessible surface area into account is found to be especially important if agglomerates contain a large number of primary particles or if the agglomerate structure is rather compact. Thus, the large particle size (agglomerate structure) favors the formation of larger particles to further reduce the surface energy [63]. However, the low-resolution SEM image (Fig. 3b) presented an assembly of groups of ultrafine particles with sizes up to 715 nm that tended to cohere into bigger particles displaying a dimension in the range of 2.11-4.52 μm, which was in good agreement with the three classes of the cumulative particle size distribution (D_{10}=610 nm, D_{50}=1.35 μm, and D_{90}=6.21 μm) of the CP-2 polishing powder (CP-2) provided by the supplier (Table I).

UV-vis DRS analysis: Fig. 4a illustrates the optical absorption spectra of CeO_2-com and CP-2 materials obtained over a wavelength range of 200-600 nm. From the curves, it is clearly shown that both materials exhibited two well-defined bands around 225 and 300 nm in the UV-visible region, accredited to the charge-transfer transition between

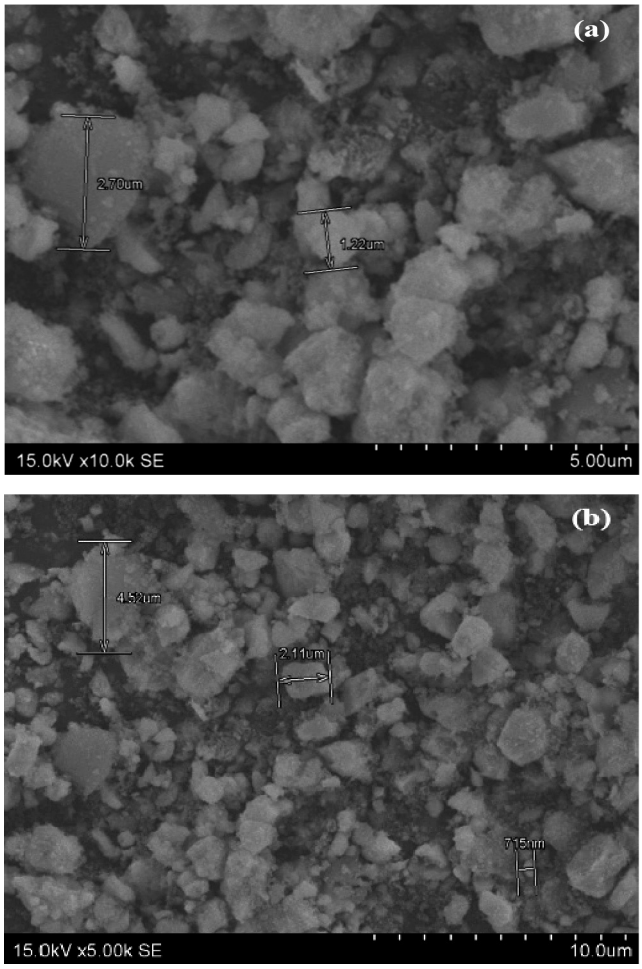

Figure 3: SEM images of CP-2 material with different magnifications.

the O 2p (full) and Ce 4f (empty) states in O^{2-} and Ce^{4+}, respectively [64]. Moreover, CP-2 displayed an absorption onset at 412 nm (E_g=3.00 eV) demonstrating the visible light stimulation of the CP-2 material. Compared with the bulk ceria (CeO_2-B, E_g=3.19 eV) and CeO_2-com (E_g=3.18 eV) [2, 65] materials, the absorption onset slightly red-shifted in CP-2 material, highlighting the presence of the rare earth compounds (La_2O_3, Pr_6O_{11}, Nd_2O_3) and F (fluorite, CaF_2, Table I), and probably the hematite (α-Fe_2O_3) phase, as evidenced by XRD observation. Such occurrence within the structure of the heterogeneous catalyst CP-2 plays a positive impact on shifting absorbance edge. These results are in good agreement with reported values in the literature [66]. The optical properties of the CeO_2-B, CeO_2-com, and CP-2

materials are reported in Table IV. The band gaps (E_g) of CeO_2-com and CP-2 materials were determined by [2, 66]:

$$\alpha h\nu \cong A(h\nu - E_g)^{n/2} \quad (H)$$

where α, h, ν, E_g, A, and n are the linear absorption coefficient, Planck's constant, light frequency, band gap energy of the material, constant, and exponent n, respectively. Fig. 4b illustrates the plots of $(\alpha h\nu)^{1/2}$ versus $h\nu$, by fitting the absorption data of CeO_2-com and CP-2 materials to the direct transition equation (n=1). As shown in Fig. 4b and reported results in Table IV, the band gap energy obtained from the intercept of the horizontal portion of the UV-vis curves with the x-axis at $(\alpha h\nu)^{1/2}=0$ gave absorption onset energies matching 3.18 and 3.00 eV for CeO_2-com and CP-2 materials, respectively, in good consistency with reported literature values [66].

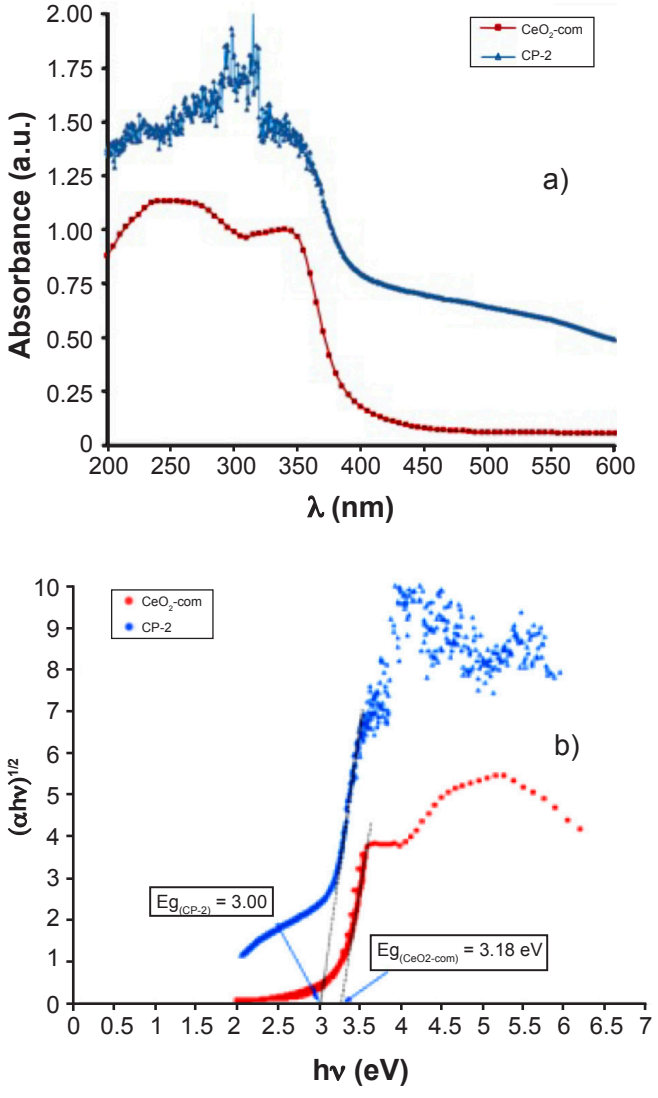

Figure 4: UV-vis DRS spectra (a) and corresponding plots of $(\alpha h\nu)^{1/2}$ against $h\nu$ (b) for CeO_2-com and CP-2 materials.

Table IV - Optical properties of CeO_2-B, CeO_2-com, and CP-2 materials.

Catalyst	λ (nm)	Charge transfer transition	Band gap E_g (eV)	
			Experimental	Literature
CeO_2-B	388.4	2p6→4f0 (Ce)	3.19	2.7-3.4 [66]
CeO_2-com	389.2		3.18	[2, 66]
CP-2	412.0		3.00	

pH point of zero charge: pH_{PZC}, an indicator of dispersion stability, is influenced by the surface chemistry that can be changed by any number of means including a change in the pH, salt concentration, surfactant concentration, and other formulation options. The pH_{PZC} measurement of the catalyst was determined by the pH drift method. The pH_{PZC} of CP-2 was carried out by adding 0.15 g of the CP-2 powder to a 50 mL solution of 0.01 M NaCl whose initial pH (pH_i) was adjusted to pH 3-11 with HCl or NaOH. The as-prepared suspensions were energetically agitated for 48 h after which the final pH (pH_f) was measured. The pH_{PZC} is defined as the point where the electrical charge density on the surface of the nanoparticles is zero. pH_{PZC} of CP-2 was obtained from the intercept of the resulting curve (ΔpH vs. pH_i) with an x-axis at $\Delta pH=0$, as illustrated in Fig. 5. The pH_{PZC} of CP-2 was found to be 6.6 in good agreement with other studies [67].

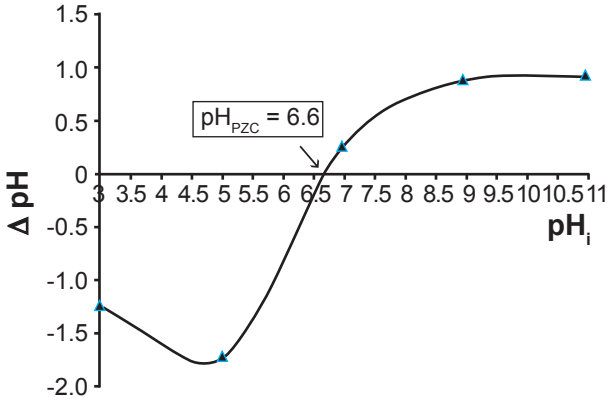

Figure 5: Graph for determination of the pH point of zero charge (pH_{PZC}) of CP-2 material.

Effect of pH: Fenton oxidation is recognized as a highly pH-dependent process. In order to find out the optimum pH solution, the effect of pH on the heterogeneous Fenton-like oxidation of NR by CP-2/H_2O_2 process was undertaken at various pH in the range of 2-12, at a fixed dye concentration (10 $mg.L^{-1}$), catalyst dosage (0.5 $g.L^{-1}$ of CP-2), H_2O_2 concentration (5 mM), and 25 °C. The results are illustrated in Figs. 6 and 7. As reported in Table V, the degradation efficiency decreased from 81.3% to 6.6% as pH was increased from 2 to 10, and then slightly raised beyond pH=10, almost reaching 36.1% at pH=12. The optimum pH was found to be 2 in which the reaction rate was the fastest, and the maximum conversion (81.3%) was achieved within 60 min. The surface complexation model or 2-pK approach was developed [68] in other to clarify the connection

between the layer charge density and the sorption/desorption reactions. In the 2-pK approach, we assume that most of the semi-conductor (SC) oxides are amphoteric in nature and can protonate or deprotonate in an aqueous solution. The pH of zero point charge (pH_{PZC}) of CP-2 was about 6.6. As a matter of fact, CP-2 material contained two surface species: CP2-Fe^{II}-H_3O^+ and CP2-Fe^{II}-O^- (CP2-Fe^{II} stands for Fe(II) sites on the CP-2 material surface). The material surface has a net positive charge at $pH<pH_{PZC}$=6.6, according to the following reaction:

$$CP2\text{-}Fe^{II} + H_2O \rightarrow CP2\text{-}Fe^{II}\text{-}H_3O^+ \quad (I)$$

CP-2 surface becomes negatively charged for pH>IEP, given by the following reaction ($pH>pH_{PZC}$):

$$CP2\text{-}Fe^{II} + H_2O \rightarrow CP2\text{-}Fe^{II}\text{-}O^- + OH^- \quad (J)$$

NR is a cationic phenazine dye that has a dimethylamino group [R-N$(CH_3)_2$Cl]. Since the pKa value is 7.1, NR dissociates to the chlorite ions Cl^- and the dimethylamino cations R-N$(CH_3)_2^+$ under acidic media (pH<7.1). It should be highlighted that, at alkali solutions (pH>7.1), most NR (conjugate base) occurs in the form of un-dissociated molecules. This means that at pH<7.1, both NR dye and CP-2 material were positively charged, resulting in greater electrostatic repulsion between the CP-2 and NR dye molecules. However, these results had a dissimilar tendency to the reported values of NR adsorption for CP-2 at pH≤6, as displayed in Table V. On the basis of the experimental results and a review of the literature [69], heterogeneous Fenton-like oxidation mechanisms of CP-2 material could be divided into two aspects: 1) the hydrogen bonding (H^+ specie) can act as a cation bridge between the positively charged CP-2 catalyst group (CP2-Fe^{II}-H_3O^+) and the nitrogen atoms [$\equiv N^+(CH_3)_3N(NH)NH_2$] of NR in cationic form possibly forming a complex [CP2-Fe^{II}-H_3O---N^+(NH)NH_2 $N^+(CH_3)_3\equiv$], facilitating greater dye adsorption:

$$CP2\text{-}Fe^{II}\text{-}H_3O^+ + \equiv N^+(CH_3)_3N(NH)NH_2 \rightarrow [CP2\text{-}Fe^{II}\text{-}H_3O\text{---}N^+(NH)NH_2N^+(CH_3)_3\equiv] \quad (K)$$

2) the decomposition of H_2O_2 over CP2-Fe^{II} was firstly initiated by the chemisorption of H_2O_2 molecules on the CP2-Fe^{II} surface, which led to the generation of the unstable CP2-$Fe^{II}(HO_2)^{2+}$ complex (Eq. L). Secondly, the decomposition of CP2-$Fe^{II}(HO_2)^{2+}$ offered the material CP2-Fe^{II} (Eq. M) for the heterogeneous Fenton-like process (Eq. N). The CP2-Fe^{II} always existed in the form of $FeOH^{2+}$, which can react

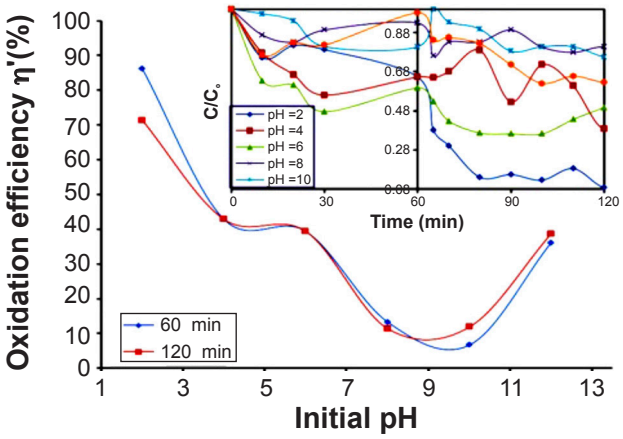

Figure 6: Effect of pH on the heterogeneous Fenton-like oxidation of NR ([CP-2]=0.5 g.L^{-1}, [NR]=10 mg.L^{-1}, [H_2O_2]=5 mM, and T=25 °C; inset: kinetics analysis for NR dye adsorption and heterogeneous Fenton-like oxidation).

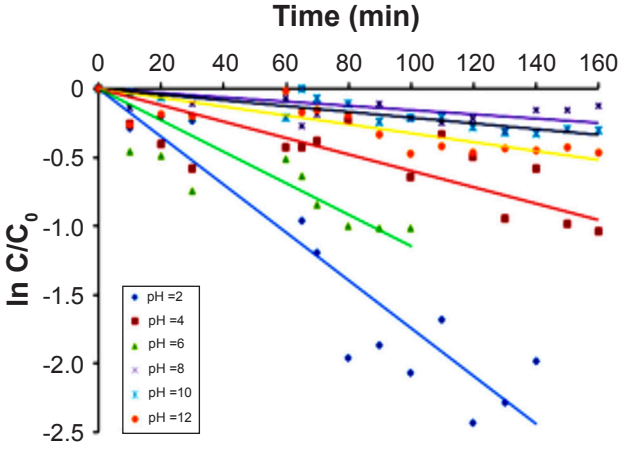

Figure 7: Pseudo-first-order kinetics for heterogeneous Fenton-like oxidation of NR at various pH solution ([CP-2]=0.5 g.L^{-1}, [NR]=10 mg.L^{-1}, [H_2O_2]=5 mM, and T=25 °C).

Table V - Pseudo-first-order kinetics parameters for heterogeneous Fenton-like oxidation of NR at various pH solution ([CP-2]=0.5 g.L^{-1}, [NR]=10 mg.L^{-1}, [H_2O_2]=5 mM, and T=25 °C).

pH	η_{60min} (%)	η'_{60min} (%)	η'_{120min} (%)	K (min^{-1})	R^2	SD
2	21.39	81.27	87.01	0.0149	0.84	0.12
4	34.63	42.85	42.85	0.0059	0.61	0.07
6	40.17	39.41	39.41	0.0114	0.56	0.07
8	7.079	13.33	11.42	0.0015	0.59	0.18
10	19.16	6.66	11.85	0.0021	0.71	0.19
12	1.89	36.12	38.70	0.0032	0.62	0.13

η: adsorption efficiency; η': oxidation efficiency; SD: standard deviation.

with H_2O_2 to form CP2-Fe^{II} (Eqs. O and P). Moreover, the Fe^{3+}/Fe^{2+} redox potential could decrease significantly by the complexed Fe^{3+}/Fe^{2+}, consequently, the Fe^{3+}/Fe^{2+} cycle was greatly boosted and more reactive oxygen species such as $^{\bullet}OH$ and $O_2^{\bullet-}/HO_2^{\bullet}$ were then produced via radical mechanism according to the Haber-Weiss mechanism (Eqs. O to Q). The organic species either can be directly oxidized by the $^{\bullet}OH$ in the solution (Eq. R) or adsorbed on the surface of the catalyst first and then oxidized.

$$CP2\text{-}Fe^{II} + H_2O_2 \rightarrow \equiv Fe(HO_2)^{2+} + H^+ \quad (L)$$

$$CP2\text{-}Fe^{II}(HO_2)^{2+} \rightarrow CP2\text{-}Fe^{II} + HO_2^{\bullet}/O_2^{\bullet-} \quad (M)$$

$$CP2\text{-}Fe^{II} + H_2O_2 \rightarrow CP2\text{-}Fe^{III} + {}^{\bullet}OH + OH^- \quad (N)$$

$$CP2\text{-}Fe^{II}OH^{2+} + H_2O_2 \rightarrow \equiv Fe(OH)(HO_2)^+ + H^+ \quad (O)$$

$$CP2\text{-}Fe^{II}(OH)(HO_2)^+ \rightarrow CP2\text{-}Fe^{II} + HO_2^{\bullet}/O_2^{\bullet} + OH^- \quad (P)$$

$$CP2\text{-}Fe^{II} + H_2O_2 \rightarrow CP2\text{-}Fe^{II} + {}^{\bullet}OH + OH^- \quad (Q)$$

$$[CP2\text{-}Fe^{II}\text{-}H_3O\text{---}N^+(NH)NH_2N^+(CH_3)_3\equiv] + {}^{\bullet}OH \rightarrow \text{reaction intermediates} \rightarrow H_2O + CO_2 \quad (R)$$

Moreover, at an acidic pH value (i.e. pH=2), a stabilized and homogeneous dispersion state of CP-2 in the bulk phase of the material was enhanced by electrostatic repulsive forces among nanoparticles. Thus, the degradation efficiency of CP-2 towards the NR was increased greatly at pH=2 by the catalytic reactions that occurred between coated iron oxides and H_2O_2 for the oxidation of NR. Additionally, when the pH solution was increased to pH_{PZC} (i.e. pH=6), the catalytic performance significantly decreased, exhibiting a degradation efficiency of 39.4%. According to general colloid chemistry principles, an electrostatically stabilized dispersion system typically loses stability when the magnitude (i.e. absolute value) of the zeta potential (i.e. the isoelectric point, or IEP) decreases to less than approximately 30 mV. As a result, there are some regions surrounding the condition of zero zeta potential (i.e. the IEP) for which the system is not particularly stable. Within this unstable region, the particles may agglomerate, thereby increasing the particle size. Moreover, the competitive reduction of ferric ions (Fe^{3+}) to ferrous ions (Fe^{2+}) realized the circulation of iron ions. However, the invalidation of Fe^{3+}/Fe^{2+} circulation resulted in not only the insufficient utilization efficiency of H_2O_2 but also the aggregation of Fe^{3+} that precipitated to form ferric hydroxide [$Fe(OH)_3$], namely iron sludge, when pH was above 3. However, when the initial pH of the NR solution was alkaline (i.e. pH= 8 and 10), a dramatic decrease in the degradation efficiency of NR could be explained on the basis of the amphoteric behavior of CP-2 catalyst and alkali media profile of NR dye and H_2O_2. In an aqueous solution, the CP-2 surfaces were negatively charged (CP2-$Fe^{II}O^-$, $pH>pH_{PZC}$=6.6, Eq. S). Thus, the molecular form of NR dye [$\equiv N(CH_3)_3N(NH)NH_2$, pH>pKa=7.1] was unable to adsorb on the surface of the CP-2 due to the electrostatic repulsion (Eq. T). Furthermore, H_2O_2 is unstable at high pH (alkaline solution), and its autodecomposition produces H_2O and O_2 and loses its oxidation ability [15], as shown in Eq. U. The activity of the heterogeneous Fenton reagent was reduced at high pH, due to the sharp decrease of reaction rate.

$$CP2\text{-}Fe^{II} + H_2O \rightarrow CP2\text{-}Fe^{II}O^- + OH^- \quad (S)$$

$$CP2\text{-}Fe^{II}\text{-}O^- + \equiv N(CH_3)_3N(NH)NH_2 \rightarrow [CP2\text{-}Fe^{II}\text{-}O^- + \equiv N(CH_3)_3N(NH)NH_2\downarrow] \quad (T)$$

$$2H_2O_2 \rightarrow O_2 + 2H_2O \quad (U)$$

On the other hand, as the solution pH increased up to 12, the degradation efficiency was raised slightly to 36.1%. As a result, the degradation extent could not be ascribed to the heterogeneous oxidation of the NR dye, but to NR dye behavior under strong alkali pH. Based on the above results, the best efficiency for heterogeneous Fenton-like process (Fe- and/or REO-CP-2/H_2O_2) was found in acidic conditions (around pH=2). Under neutral and basic pH conditions, H_2O_2 formed very stable peroxide-like species (OOH^-) with cerium and these species did not decompose thus, no $^{\bullet}OH$ radicals were generated at all because of the redox cycle between Ce^{4+}/Ce^{3+} was completely blocked. Accordingly, all additional research was carried out at a pH=2. Furthermore, the first-order kinetic model for the heterogeneous Fenton-like oxidation of NR over CP-2 at various pH solutions was explored by plotting $\ln(C/C_0)$ vs. time (Fig. 7). It was observed that the heterogeneous oxidation rate could be fitted to pseudo-first-order kinetics with fairly good correlation coefficients ($0.59 \leq R^2 \leq 0.84$). The apparent reaction rate constant and R^2 are displayed in Table V.

Effect of H_2O_2: the hydrogen peroxide (H_2O_2) is a key parameter that significantly impacts the Fenton reactions. The effect of H_2O_2 concentration on the degradation of NR over the CP-2/H_2O_2 system was investigated in the range of 2.5 to 25 mM while keeping the dye concentration, material dosage, temperature, and natural pH at 10 $mg.L^{-1}$, 0.5 $g.L^{-1}$, 25 °C, and pH=6 (for this experiment only), respectively. From Fig. 8, it is seen that the heterogeneous Fenton-like reaction is relatively sensitive to the H_2O_2 concentration. It was observed that the degradation process was practically steady and the degradation efficiency varied from 67.4% to 63.0% with the increase in the H_2O_2 concentration from 2.5 to 10 mM, at a reaction time of 60 min. However, the dye degradation efficiency was scarily reduced beyond the H_2O_2 concentration of 10 mM, achieving almost 24.6% at 25 mM of H_2O_2 (Table VI), highlighting a negative impact on the degradation of the dye. At low H_2O_2 concentrations (i.e. 2.5-10 mM), the decomposition of dissolved H_2O_2 on the catalyst surface of CP-2 was significant, producing high hydroxyl radicals ($^{\bullet}OH$), which improved the rate of oxidation and the degradation efficiency according to [70]:

$$CP2\text{-}Fe^{II}\ sites + H_2O_2 \rightarrow CP2\text{-}Fe^{II}\ sites\ H_2O_2 \quad (V)$$

$$CP2\text{-}Fe^{II}\ sites\ H_2O_2 \rightarrow CP2\text{-}Fe^{II}\ sites + HO_2^{\bullet} + H^+ \quad (W)$$

$$CP2\text{-}Fe^{II}\ sites + H_2O_2 \rightarrow CP2\text{-}Fe^{II}\ sites + {}^{\bullet}OH + OH^- \quad (X)$$

However, with further H_2O_2 concentration increase beyond 10 mM, the degradation efficiency of CP-2 catalyst considerably declined to 24.6% at an H_2O_2 concentration of 25 mM. This phenomenon could be explained by three possible reasons. First, is the generation of hydroperoxyl radicals ($HO_2^{\bullet}$), which act as scavengers of hydroxyl radicals (Eq. Y). Second, the hydroperoxyl radicals exhibited much lower oxidation capabilities and did not contribute to the NR degradation (Eq. Z), which resulted in a decrease in the degradation efficiency. Third, the radical-radical reaction (Eq. AA) may occur in competition with radical-organic reactions, thus leading to more consumption of ${}^{\bullet}OH$, which would not be consumed by the dye. Based on our obtained results, 5 mM of H_2O_2 was used as the optimum concentration in subsequent experiments.

$$H_2O_2 + {}^{\bullet}OH \rightarrow H_2O + HO_2^{\bullet} \quad (Y)$$

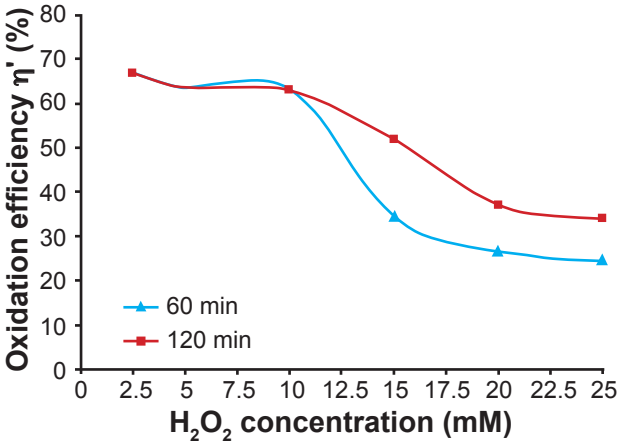

Figure 8: Effect of H_2O_2 concentration on the heterogeneous Fenton-like oxidation of NR ([CP-2]=0.5 g.L^{-1}, [NR]=10 mg.L^{-1}, pH=6, and T=25 °C).

Table VI - Results of effect of H_2O_2 concentration on the heterogeneous Fenton-like oxidation of NR ([CP-2]=0.5 g.L^{-1}, [NR]=10 mg.L^{-1}, pH=6, and T=25 °C).

H_2O_2 concentration (mM)	η_{60min} (%)	η'_{60min} (%)	η'_{120min} (%)
2.5	52.83	66.81	66.81
5	40.17	63.60	63.60
10	55.02	62.99	62.99
15	23.30	34.17	51.89
20	43.68	26.72	37.06
25	38.83	24.60	34.12

η: adsorption efficiency; η': oxidation efficiency.

$$HO_2^{\bullet} + {}^{\bullet}OH \rightarrow H_2O + O_2 \quad (Z)$$

$${}^{\bullet}OH + {}^{\bullet}OH \rightarrow H_2O_2 \quad (AA)$$

Effect of the initial NR concentration: to investigate the effect of initial dye concentration on the heterogeneous Fenton-like oxidation of NR by CP-2 material in the presence of H_2O_2, various tests with NR initial concentrations at 10, 20, 40, 50, and 60 mg.L^{-1} were carried out. All experiments were performed at an H_2O_2 concentration of 5.0 mM, CP-2 material dosage of 0.5 g.L^{-1}, 25 °C, pH 2, and reaction times of 60 and 120 min. As shown in Fig. 9, the oxidation kinetics of the NR via the heterogeneous Fenton-like process (CP-2/H_2O_2 system) decreased with time and then achieved equilibrium after 60 min. The degradation efficiency was almost steady as the initial NR concentration was increased from 10 to 20 mg.L^{-1} and then considerably decreased beyond 20 mg.L^{-1}. However, for the reaction time of 120 min, an obvious decline in the degradation efficiency from 87.0% to 1.8% as the initial NR concentration was increased from 10 to 50 mg.L^{-1}. The highest efficiency of 81.3% and 87.0% were achieved within 60 and 120 min of reaction time. This highlight may be caused by the self-scavenging effect of ${}^{\bullet}OH$ by the concurrent Fe^{3+} in the CP-2 matrix, according to Eqs. AB and AC, as well as the decrease in the driving force of concentration gradient with the increase in the quantity of dye molecules per volume unit. Furthermore, the molar ratio of oxidant/NR was 0.14, 0.07, and 0.02, respectively, for 10, 20, and 60 mg.L^{-1}, an increase in the NR concentration competing with the number of ${}^{\bullet}OH$ radicals in the solution. It is important to highlight that a lower oxidant H_2O_2/NR dye molar ratio was unfavorable in the CP-2 heterogeneous Fenton-like system, which may be due to the limited generation rate of ${}^{\bullet}OH$ radicals in the solution. Therefore, 10 mg.L^{-1} of NR was selected as the dye concentration for the following experiments.

$$CP2\text{-}Fe^{II+} + {}^{\bullet}OH \rightarrow CP2\text{-}Fe^{III+} + OH^- \quad (AB)$$

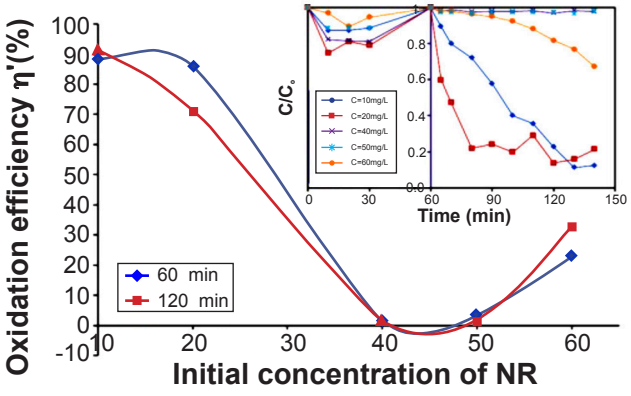

Figure 9: Effect of initial NR concentration on the heterogeneous Fenton-like oxidation of NR ([CP-2]=0.5 g.L^{-1}, [H_2O_2]=5 mM, pH=2, and T=25 °C; inset: kinetics analysis for NR dye adsorption and heterogeneous Fenton-like oxidation).

$$CP2\text{-}Fe^{II+} + {}^{\bullet}OOH \rightarrow CP2\text{-}Fe^{III+} + OOH^{-} \quad (AC)$$

Moreover, the heterogeneous Fenton-like oxidation data were carried out under pseudo-first-order model conditions and the results are shown in Fig. 10. The corresponding K values were assessed to be 0.0149, 0.0205, 0.0003, 0.0004, and 0.0025 min^{-1} for 10, 20, 40, 50, and 60 $mg.L^{-1}$ NR, respectively (Table VII). The K values of the CP-2 material were maximum as the initial concentrations of NR were laid between 10-20 $mg.L^{-1}$ NR, indicating that the heterogeneous Fenton-like oxidation process was improved through low initial NR dye concentrations.

Effect of catalyst dosage: the influence of the catalyst dosage on the degradation of NR was studied by varying the catalyst dosage from 0.5 to 1.5 $g.L^{-1}$ while keeping constant all the other operating parameters (initial NR concentration of 10 $mg.L^{-1}$, H_2O_2 concentration of 5.00 mM, pH 2, and 25 °C). Table VIII summarizes the results of the effect of CP-2 dosage on the heterogeneous oxidation of NR. According to the results presented in Fig. 11, the degradation of NR was scarily reduced from 81.3% to 5.8% as the dosage of catalyst raised from 0.5 to 0.75 $g.L^{-1}$. The drastic decline in the degradation process response would lead to less production of the available iron active sites on the surface of the catalyst for the activation of H_2O_2 to generate more free reactive hydroxyl radicals ($^{\bullet}OH$), thus reducing the degradation response in the proposed heterogeneous Fenton-like process. However, for further increase in catalyst dosage beyond 0.75 $g.L^{-1}$, the degradation response was slightly increased, almost reaching 8.5% for 1.5 $g.L^{-1}$ of catalyst dose. This highlight may be attributed to the increase in the rate of decomposition of H_2O_2 to O_2 owing to thermodynamic and mass transfer limitations and also the scavenging effect of $^{\bullet}OH$ radicals by the excess Fe(II) ions on the surface of the catalyst (Eqs. AD and AE) [71]. Thus, nearly 81.3% and 87.0% degradation responses were achieved within 60 and 120 min, respectively, with the optimum catalyst dosage of 0.5 g/L in the heterogeneous Fenton-like reaction. Thus, 0.5 $g.L^{-1}$ of CP-2 was selected as the catalyst dosage for the subsequent experiments.

$$CP2\text{-}Fe^{II} \text{ sites} + {}^{\bullet}OH \rightarrow CP2\text{-}Fe^{II} \text{ sites} + OH^{-} \quad (AD)$$

$$CP2\text{-}Fe^{II} \text{ sites} + {}^{\bullet}OOH \rightarrow CP2\text{-}Fe^{II} \text{ sites} + OOH^{-} \quad (AE)$$

Effect of temperature: to understand the effect of temperature, the heterogeneous oxidation studies were investigated by varying the temperature from 25 to 60 °C, at a fixed dye concentration of 10 $mg.L^{-1}$, H_2O_2 concentration of

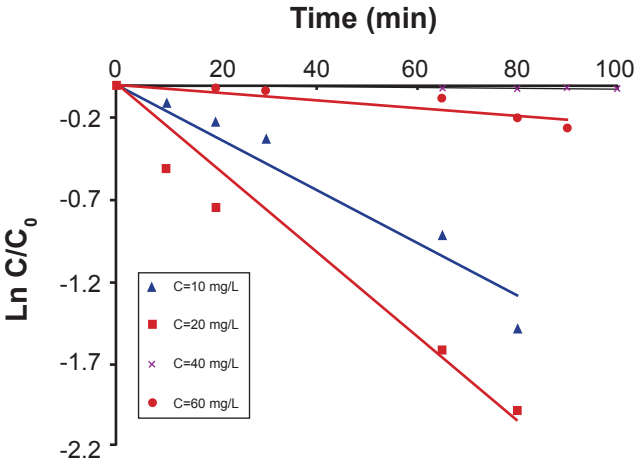

Figure 10: Pseudo-first-order kinetics for heterogeneous Fenton-like oxidation of NR at various initial NR concentrations ([CP-2]=0.5 $g.L^{-1}$, [H_2O_2]=5 mM, pH=2, and T=25 °C).

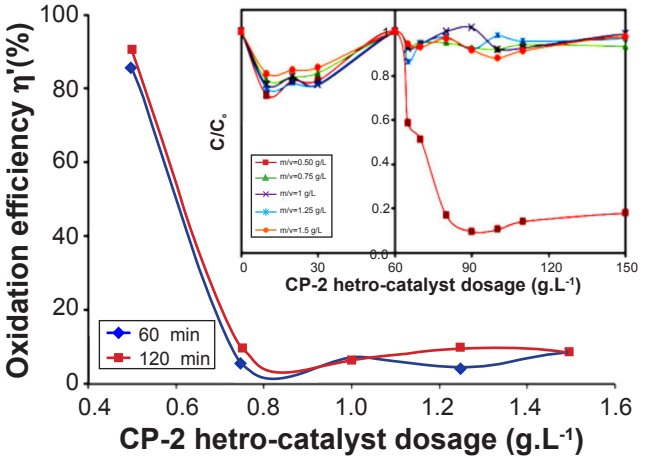

Figure 11: Effect of CP-2 dosage on the heterogeneous Fenton-like oxidation of NR ([NR]=10 $mg.L^{-1}$, [H_2O_2]=5 mM, pH=2, and T=25 °C; inset: kinetics analysis for NR dye adsorption and heterogeneous Fenton-like oxidation).

Table VII - Pseudo-first-order kinetics parameters for heterogeneous Fenton-like oxidation of NR at various initial NR concentrations ([CP-2]=0.5 $g.L^{-1}$, [H_2O_2]=5 mM, pH=2, and T=25 °C).

C ($mg.L^{-1}$)	η_{60min} (%)	η'_{60min} (%)	η'_{120min} (%)	K (min^{-1})	R^2	SD
10	21.39	81.27	87.01	0.0149	0.84	0.12
20	36.36	85.90	71.42	0.0205	0.78	0.11
40	18.01	1.65	2.25	0.0003	-	0.31
50	9.92	3.37	1.83	0.0004	-	0.32
60	7.26	23.08	32.83	0.0025	0.70	0.27

η: adsorption efficiency; η': oxidation efficiency; SD: standard deviation.

Table VIII - Results of the effect of CP-2 dosage on the heterogeneous Fenton-like oxidation of NR ([NR]=10 mg.L^{-1}, [H_2O_2]=5 mM, pH=2, and T=25 °C).

Catalyst dosage (g.L^{-1})	η_{60min} (%)	η'_{60min} (%)	η'_{120min} (%)
0.50	21.39	81.27	87.01
0.75	18.81	5.79	9.43
1.00	22.71	7.30	6.78
1.25	20.56	4.23	9.81
1.50	13.57	8.55	8.55

η: adsorption efficiency; η': oxidation efficiency.

5.0 mM, and pH 2. Fig. 12 depicts the plot of heterogeneous oxidation of NR dye as a function of reaction time at various temperatures. It should be noted that a higher temperature enhances the rate of formation of •OH radicals according to Arrhenius law, but also favors the decomposition of hydrogen peroxide into oxygen and water, which reduces the efficiency of the heterogeneous Fenton process. In addition, with gradually increasing the temperature, the rate of diffusion of the adsorbate molecules across the external boundary layer and in the internal pores of the adsorbent particle was increased, owing to the decrease in the viscosity of the solution [72]. Indeed, once the temperature was increased from 25 to 40 °C, the adsorption rate of NR onto CP-2 catalyst increased from 19.1% to 81.3%, suggesting the endothermic nature of the adsorption reaction, while it slightly decreased up to 55.4% at 60 °C. On the other hand, the heterogeneous oxidation of NR by the CP-2/H_2O_2 system proceeded with two main oxidation stages. The first oxidation stage occurred from 0-60 min, corresponding to the slight increase in the heterogeneous oxidation of NR from 60.0% to 81.3% as the temperature was increased from 25 to 40 °C and slightly leveled off when the temperature was raised up to 60 °C, almost reaching 66.1%. In the exposure time range of 60-120 min, a second oxidation stage was observed, corresponding to a drastic decline in the heterogeneous oxidation of NR by the CP-2/H_2O_2 process from 87.0% to 33.9% when the temperature was increased from 25 to 40 °C, while it increased from 33.9% to 67.7% with the increase in temperature up to 60 °C. Three possible reasons could explain the second oxidation stage behavior. First, it could be attributed to the decreased oxygen solubility in water [73]. The second reason would be the non-stability of H_2O_2 at a high temperature, more than 40 °C, which could affect the degradation efficiency of the catalyst through its autodecomposition to give H_2O and O_2 (Eq. AF) [74]. The third reason could be ascribed to the fact that the oxidant H_2O_2/NR dye molar ratios at elevated temperature (i.e. 40 °C) are three times higher than that corresponding to the optimal condition (i.e. 25 °C), leading to the limited formation of •OH radicals in the solution as a result of a scavenging effect of hydroxyl radicals by the hydroperoxyl radicals (HO_2•).

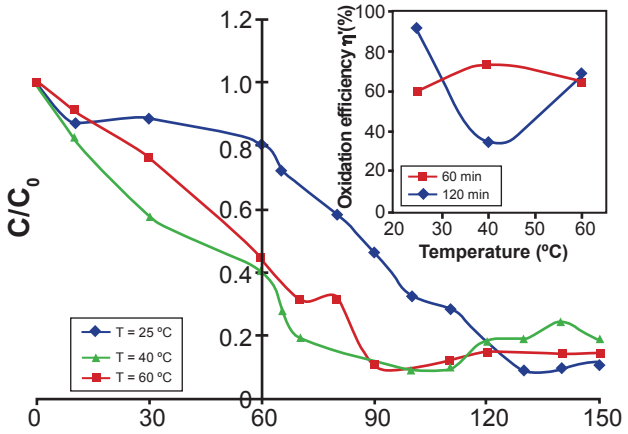

Figure 12: Kinetics analysis for NR dye adsorption and heterogeneous Fenton-like oxidation of NR at various medium temperatures ([CP-2]=0.5 g.L^{-1}, [NR]=10 mg.L^{-1}, [H_2O_2]=5 mM, and pH=2; inset: effect of temperature on the heterogeneous oxidation efficiency of NR by CP-2 catalyst).

$$2H_2O_2 \rightarrow O_2 + 2H_2O \qquad (AF)$$

However, considering the degradation efficiency and thermal energy supply in the form of heat, 25 °C was selected as the optimal operating temperature in the further experiments. In this study, the pseudo-first-order model was used to describe the heterogeneous Fenton-like process at various temperatures. The plot of ln(C/C_0) vs. time (t) was a straight line, as illustrated in Fig. 13. This suggested that the heterogeneous oxidation of NR dye at different temperatures followed a pseudo-first-order rate law. The rate constants were found to be 0.0149, 0.0141, and 0.021 min^{-1} for 25, 40, and 60 °C, respectively. The coefficients of determination R^2 obtained from the linear regression were found to be greater than 0.84 for temperatures higher than 25°C. The data obtained for the kinetics experiment are shown in Table IX.

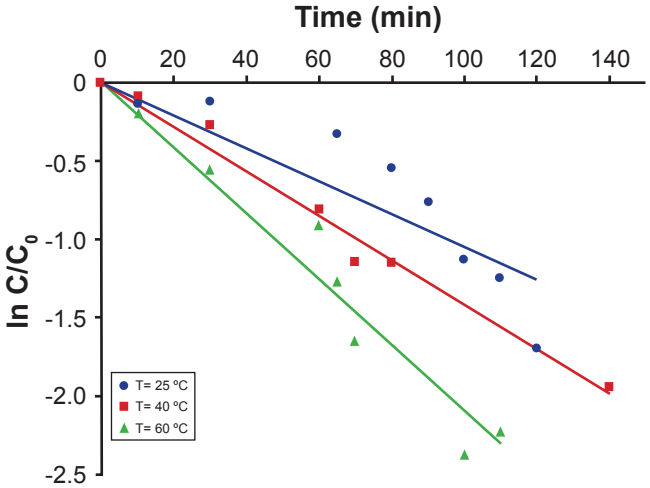

Figure 13: Pseudo-first-order kinetics for heterogeneous Fenton-like oxidation of NR at various temperature ([CP-2]=0.5 g.L^{-1}, [NR]=10 mg.L^{-1}, [H_2O_2]=5 mM, and pH=2).

Table IX - Pseudo-first-order kinetics parameters for heterogeneous Fenton-like oxidation of NR at various temperatures ([CP-2]=0.5 g.L^{-1}, [NR]=10 mg.L^{-1}, [H_2O_2]=5 mM, and pH=2).

T (°C)	η_{60min} (%)	η'_{60min} (%)	η'_{120min} (%)	K (min^{-1})	R^2	SD
25	21.39	81.27	87.01	0.0149	0.84	0.12
40	59.72	73.21	33.92	0.0141	0.98	0.07
60	55.40	66.12	67.74	0.0210	0.95	0.10

η: adsorption efficiency; η': oxidation efficiency; SD: standard deviation.

Thermodynamic study: to investigate the effect of reaction temperature on the NR Fenton-like oxidation, kinetic data were performed at three different temperatures (25, 40, and 60 °C). The rate constant K value gradually rose with the increase of temperature from 25 to 60 °C, as shown in Fig. 14a. The apparent activation energy (E_a, kJ.mol^{-1}) for heterogeneous Fenton-like oxidation of NR at various temperatures was computed with the Arrhenius equation:

$$K = A.e^{\left(\frac{-Ea}{R.T}\right)} \quad (AG)$$

where A is the pre-exponential factor, R (8.314 J.mol^{-1}.K^{-1}) is the ideal gas constant, and T (K) is the reaction absolute temperature. As shown in Fig. 14a, the Arrhenius plot of lnK against 1/T exhibited a good linear relationship (R^2=0.9988). From the slope of the line, E_a was obtained. The E_a of ordinary thermal reactions is usually between 60 and 250 kJ.mol^{-1} in general [75], so the E_a value of 16.4 kJ.mol^{-1} indicated that the reduction of NR by the heterogeneous Fenton-like reaction proceeded with a low energy barrier. Rate constants may also be related to energy changes by the general form of the Eyring-Polanyi equation (from transition state theory) [76], which somewhat resembles the Arrhenius equation as shown in Eq. AH:

$$K = \frac{K_B.T}{h} e^{\left(\frac{-\Delta G^{\ddagger}}{R.T}\right)} \quad (AH)$$

and $\Delta G^{\ddagger}$ is the free energy activation (Gibb's free energy) given by:

$$\Delta G^{\ddagger} = \Delta H^{\ddagger} - T.\Delta S^{\ddagger} \quad (AI)$$

where K_B is the Boltzmann's constant ($1.381x10^{-23}$ J.K^{-1}), h is the Planck's constant ($6.626x10^{-34}$ J.s), $\Delta H^{\ddagger}$ (kJ.mol^{-1}) is the enthalpy of activation, and $\Delta S^{\ddagger}$ (J.mol^{-1}.K^{-1}) is the entropy of activation. The linear Eyring-Polanyi equation is given by:

$$\ln\frac{K}{T} = \frac{-\Delta H^{\ddagger}}{R}\frac{1}{T} + \ln\frac{K_B}{h} + \frac{\Delta S^{\ddagger}}{R} \quad (AJ)$$

The values for $\Delta H^{\ddagger}$ and $\Delta S^{\ddagger}$ can be determined from kinetic data obtained from an ln(K/T) vs. 1/T plot (Fig. 14b). The Eq. AJ is a straight line with a negative slope of $-\Delta H^{\ddagger}/R$ and a y-intercept of $\ln k_B/h+\Delta S^{\ddagger}/R$. The enthalpy of activation ($\Delta H^{\ddagger}$) was found to be 13.7 kJ.mol^{-1} and the positive value of the enthalpy showed that the Fenton-like reaction was endothermic in nature. The entropy of activation ($\Delta S^{\ddagger}$) was -236.7 J.mol^{-1}.K^{-1} and this negative value implied that the activated complex in the transition state had a more ordered or more rigid structure than the reactants in the ground state. This is generally the case if degrees of freedom (translation, rotation, vibration) become 'frozen' on the route from the initial to the transition state. The reaction rate was slow. The values of Gibb's free energy of activation ($\Delta G^{\ddagger}$), which is considered a driving force of the Fenton reaction, determine the extent and spontaneity of the reaction. $\Delta G^{\ddagger}$ was calculated from the enthalpy and the entropy of activation at different temperatures. The values were found to be 84.3, 87.8, and 92.6 kJ/mol at 298, 313, and 333 K, respectively. The large negative values of $\Delta G^{\ddagger}$ implied that the oxidative reaction

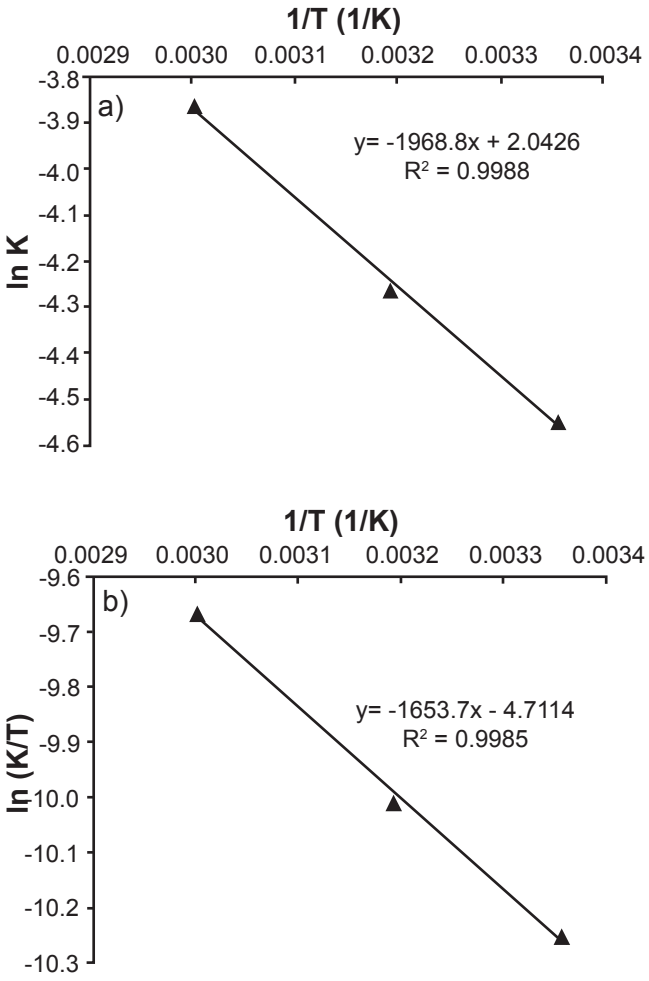

Figure 14: Plots of lnK (a) and ln(K/T) (b) versus 1/T for the heterogeneous Fenton-like oxidation of NR at various temperatures.

using the Fenton reagent for the degradation of NR was not spontaneous and unfavorable.

Effect of inorganic anion content: dissolved inorganic and organic compounds exist in dye-containing industrial wastewater or underground water. Most of these substances are used for adjustment of pH in the dye bath, stabilization of the dye molecules on the fibers, and improvement of color stability. Their presences usually affect the oxidation efficiency of the Fenton process. Therefore, the degradation rates of the target dye decrease. It is well-known that •OH, as the predominant radical, is reportedly generated through Fenton-like reactions. •OH radicals react with non-target compounds present in the background water such as dye auxiliaries present in the dye bath. They cause higher •OH demand to achieve the desired degree of degradation or complete inhibition of advanced degradation rate and efficiency [77]. To understand the impact of the inorganic salt on the heterogeneous Fenton-like processes using CP-2 catalyst, we applied sodium chloride (NaCl) as specific scavengers of hydroxyl radicals and the results are illustrated in Fig. 15. As observed, the anionic species studied had an inhibitory effect in the heterogeneous Fenton-like system (Fe- and/or REO-CP-2/H_2O_2). NR degradation efficiency was declined from 81.3%, in the absence of scavenger, to 69.1% and ≅10.8% in the presence of NaCl mass at 1 and ≥2 g, respectively, which implied that •OH radicals might be the prominent active reactive oxygen species (ROS) involved in the NR oxidation via Fe- and/or REO-CP-2/H_2O_2 process. The discrepancy in degradation efficiency observed for the whole NaCl mass can be explained on the basis of two aspects. First, chloride anions (Cl^-) compete with a cationic form of NR dye for active catalytic sites available on the CP-2 surface (Eqs. AK and AL), resulting in a reduction in both the adsorption extent and surface catalytic activity of CP-2. Second, Cl^- anions react with •OH radicals, through their scavenging effects, forming less oxidative species such as Cl• (Eq. AM).

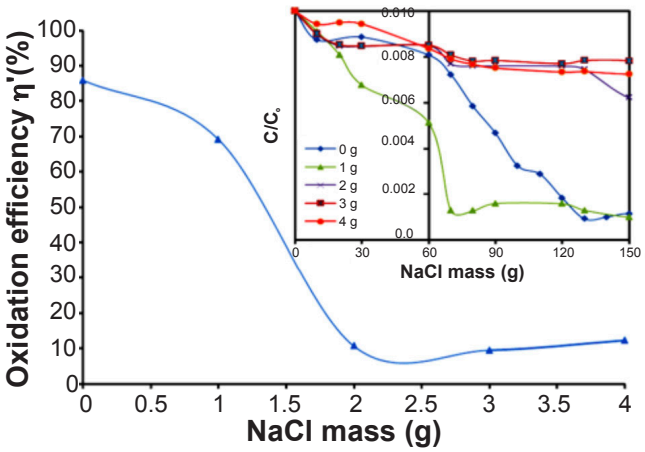

Figure 15: Effect of inorganic anion content on the heterogeneous Fenton-like oxidation of NR ([CP-2]=0.5 g.L^{-1}, [NR]=10 mg.L^{-1}, [H_2O_2]=5 mM, pH=2, and T=25 °C; inset: kinetics analysis for NR dye adsorption and heterogeneous Fenton-like oxidation).

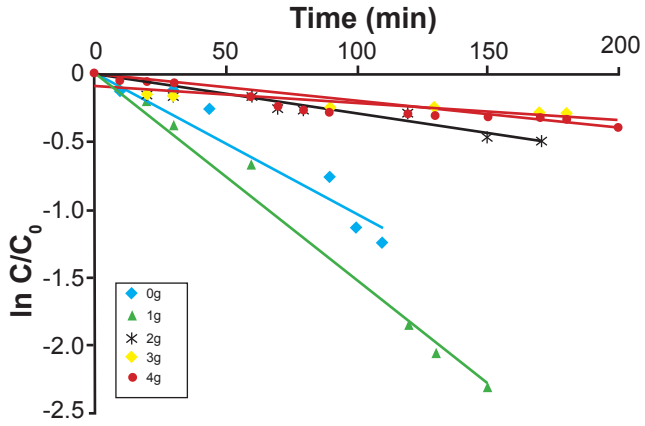

Figure 16: Pseudo-first-order kinetics for heterogeneous Fenton-like oxidation of NR at various inorganic anion contents ([CP-2]=0.5 g.L^{-1}, [NR]=10 mg.L^{-1}, [H_2O_2]=5 mM, pH=2, and T=25 °C).

$$CP2\text{-}Fe^{II}sites\text{-}H_3O^+ + \equiv N^+(CH_3)_3N(NH)NH_2 \rightarrow [CP2\text{-}Fe^{II}sites\text{-}H_3O\text{---}N^+(NH)NH_2N^+(CH_3)_3\equiv] \quad (AK)$$

$$CP2\text{-}Fe^{II}sites\text{-}H_3O^+ + Cl^- \rightarrow [CP2\text{-}Fe^{II}sites\text{-}H_3O\text{-----}Cl] \quad (AL)$$

$$^{\bullet}OH + Cl^- \rightarrow OH^- + Cl^{\bullet} \quad (AM)$$

The observed data were also analyzed by the pseudo-first-order model. The regression of the plot of ln(C/C_0) vs. time (Fig. 16) was linear suggesting that the oxidation of NR through a heterogeneous Fenton-like process at various NaCl masses was best described by the pseudo-first-order model. Moreover, the coefficients of determination R^2 were

Table X - Pseudo-first-order kinetics parameters for heterogeneous Fenton-like oxidation of NR at various inorganic anion contents ([CP-2]=0.5 g.L^{-1}, [NR]=10 mg.L^{-1}, [H_2O_2]=5, pH=2, and T=25 °C).

NaCl mass (g)	η_{60min} (%)	η'_{60min} (%)	η'_{120min} (%)	K (min^{-1})	R^2	SD
0	21.39	81.27	87.01	0.0149	0.84	0.12
1	48.73	69.13	82.72	0.0149	0.79	0.12
2	15.03	10.61	59.59	0.0039	0.75	0.15
3	14.87	9.47	20.63	0.0020	0.61	0.19
4	16.29	12.28	19.28	0.0022	0.83	0.19

η: adsorption efficiency; η': oxidation efficiency; SD: standard deviation.

found to lie between 0.61 and 0.84 (Table X).

Comparative study: in this part of the work, three sets of experiments were performed in the following catalytic processes conditions: CP-2 material catalyst only (adsorption process), H_2O_2 only (homogeneous oxidation process), and CP-2 catalyst along with hydrogen peroxide H_2O_2 (heterogeneous Fenton-like process), as shown in Fig. 17 and reported results in Table XI. In the case of the homogeneous oxidation system, only 1.0% of dye degradation was achieved within 60 min of reaction. For the adsorption process, 21.4% dye removal was obtained. However, significant degradation efficiency was only observed for the heterogeneous Fenton-like process with 81.3% of dye degradation at the same reaction time. The enhanced heterogeneous Fenton-like oxidation CP-2 catalyst towards NR dye could be mainly attributed to the synergetic

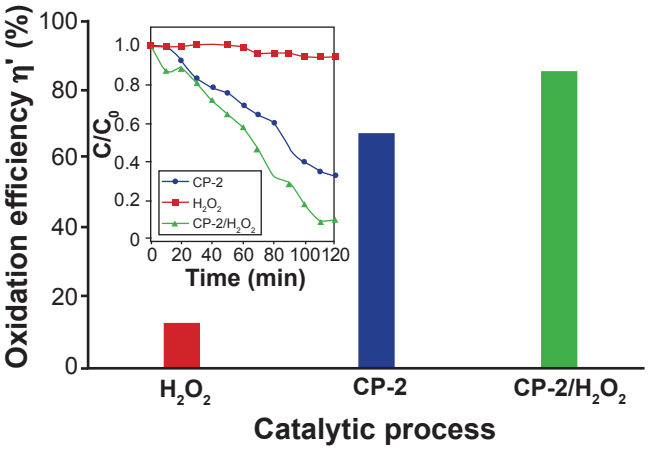

Figure 17: Effect of the different catalytic processes on the oxidation efficiency of NR ([CP-2]=0.5 g.L^{-1}, [NR]=10 mg.L^{-1}, [H_2O_2]=5 mM, pH=2, and T=25 °C; inset: kinetics analysis for NR dye adsorption, homogeneous oxidation, and heterogeneous Fenton-like oxidation processes NR).

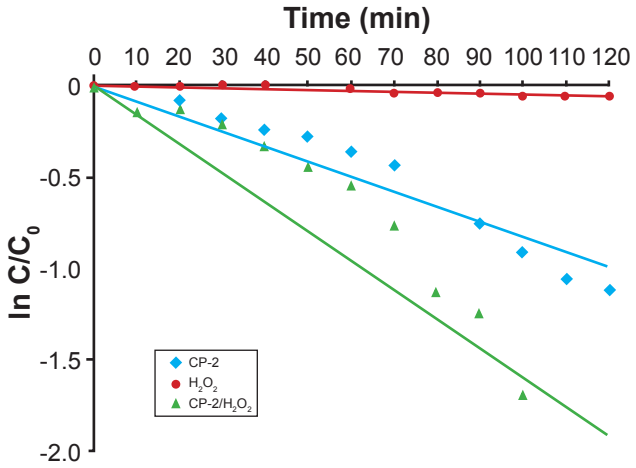

Figure 18: Pseudo-first-order kinetics for various catalytic processes ([CP-2]=0.5 g.L^{-1}, [NR]=10 mg.L^{-1}, [H_2O_2]=5 mM, pH=2, and T=25 °C).

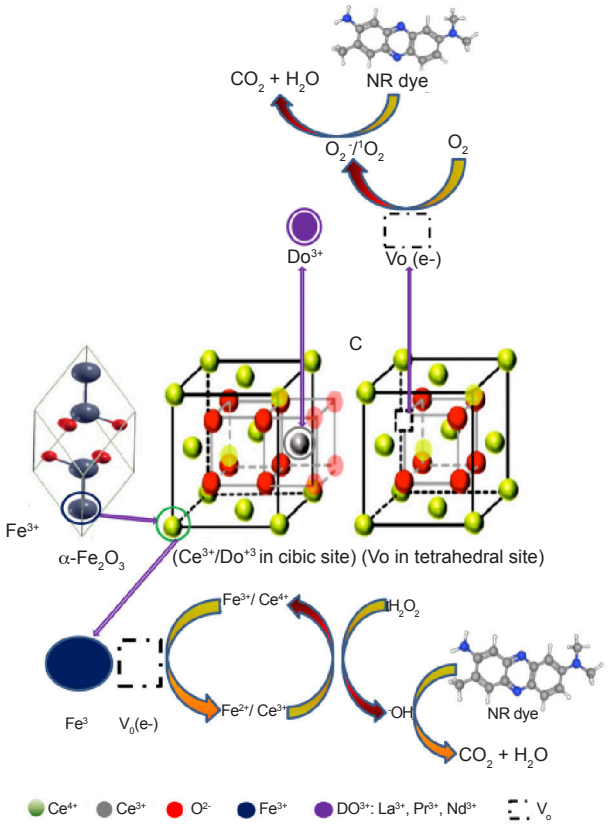

Figure 19: Plausible mechanisms of heterogeneous Fenton-like reaction over α-Fe_2O_3/REO-CP-2/H_2O_2 system.

Table XI - Pseudo-first-order kinetics parameters for various catalytic processes ([CP-2]=0.5 g.L^{-1}, [NR]=10 mg.L^{-1}, [H_2O_2]=5 mM, pH=2, and T=25 °C).

Abbreviation	Catalytic process	η (%)		η' (%)		K (min^{-1})	R^2
		60 min	120 min	60 min	120 min		
H_2O_2	Homogeneous oxidation process (H_2O_2 only)	-	-	1.00	5.60	0.0004	0.70
CP-2	Adsorption process (CP-2 catalyst only)	21.39	67.36	-	-	-	-
CP-2/H_2O_2	Heterogeneous Fenton-like process (CP-2/H_2O_2)	-	-	81.27	87.01	0.0149	0.84

η: adsorption efficiency; η': oxidation efficiency.

catalysis of H_2O_2 by Fe^{3+}/Fe^{2+} and Ce^{3+}/Ce^{4+} redox couples, which generated more $^{\bullet}OH$ radicals, causing a high response in degradation process [78, 79]. Fig. 18 depicts the time (t) dependence of $\ln(C/C_0)$ on the degradation of NR dye in various catalytic processes. A linear variation of $\ln(C/C_0)$ was observed for all of the catalytic processes, indicating a typical first-order reaction ($R^2 \geq 70$). The kinetics data obtained from the linear regression are presented in Table XI. The rate constants K were assessed to be 0.0004 min^{-1} for the homogeneous oxidation process (H_2O_2 only) and 0.0149 min^{-1} for the heterogeneous Fenton-like process employing iron-based catalyst (CP-2/H_2O_2 system).

Potential mechanism of NR heterogeneous Fenton-like process: a potential degradation mechanism of phenazine dye over the α-Fe_2O_3/REO-CeO_2/H_2O_2 system is proposed in Fig. 19. The enhanced heterogeneous Fenton-like oxidation of NR dye over the α-Fe_2O_3/REO-CeO_2/H_2O_2 system could be mainly ascribed to the heterogeneous Fenton reaction promoted by oxygen vacancies. Fenton reaction can be performed through activation of hydrogen peroxide (H_2O_2), as an oxidant, and the couple of Fe^{2+}/Fe^{3+}, as a catalyst, according to Eqs. AN and AO. Owing to its oxidation properties, cerium can conveniently produce $^{\bullet}OH$ from H_2O_2 due to the exhibition of two oxidation states, i.e., the Ce^{3+} and Ce^{4+}. Heckert et al. [80] used cerium-based heterogeneous catalysts for the production of $^{\bullet}OH$ and $HO_2^{\bullet}$ from H_2O_2 through the mechanism outlined in Eqs. AP and AQ. In the other way, the generation of $^{\bullet}OH$ and $HO_2^{\bullet}$ free radicals take place through H_2O_2 catalyzed by the couple of Ce^{4+}/Ce^{3+} via the Fenton-like reaction. Moreover, the synergistic iron and ceria interaction (Eq. AR) can facilitate the redox cycles of Fe^{3+}/Ce^{4+} and Fe^{2+}/Ce^{3+}. During the recombination of free

Table XII - Cerium-based catalysts employed in heterogeneous Fenton-like oxidation.

Catalyst composition	Catalyst dose (g/L)	H_2O_2 dose (mM/L)	pH	T (°C) (time)	Target compound	Degradation (%)	Mineralization (%)	Ref.
CeO_2-$LaCuO_3$	0.4	12.5	7	25 (6 h)	Bisphenol	99.85	72.44	[86]
Ce-Cu oxide composite	1	-	4	50 (2 h)	2,4-dichlorophenol	99.5	82	[87]
Fe_3O_4/CeO_2	2	30	2	30 (1.5 h)	2,4,6-trichlorophenol	99	65	[88]
CeO_2	0.5	10	-	25 (8 h)	Acid Orange 7	98	-	[89]
Ce-Cu oxide composite	1	-	4	50 (2 h)	4-chlorophenol (4-CP)	95	88	[87]
Ce_xCuO_y	0.1	50	5	25 (1 h)	Fluconazole	94	-	[90]
CeO_2	1	18	-	25 (5 h)	Acid Orange 7	90	-	[91]
Fe^0/CeO_2	0.1	100	5.8	26 (1 h)	Tetracycline	90	-	[92]
$FeCeO_x$	1.5	80	5	35 (2.5 h)	Rhodamine B	90	-	[93]
CeO_2	1.5	60	5	22 (2 h)	Orange II	85	-	[94]
CeO_2	1.5	116	3	22 (2 h)	Acid green	60	-	[94]
Fe_2O_3-CeO_2	0.5	8	3	45 (2 h)	Sulfamerazine	70	-	[52]
CuO/CeO_2	1.2	200 mg/L		25 (1 h)	Diclofenac	86.62	-	[54]
PB/CeO_2	0.0005	15	4	25 (1 h)	Norfloxacin	95.32	-	[95]
Fe_3O_4/CeO_2	2	30	3.3	35 (2 h)	Pantoprazole	98	-	[96]
Fe_3O_4/CeO_2	2	30	2.5	35 (2 h)	Orange G	98.2	-	[97]
FeCeOx	0.5	3	5	25 (40 min)	Diclofenac	84	-	[98]
CuO-CeO_2-Fe_2O_3/ATP	5	4.9	5	60 (1 h)	Methylene blue	99.83	-	[99]
FeNiCeOx	1	9.8	5	25 (30 min)	Diclofenac	97.9	-	[100]
Fe/CeO_2-TiO_2	30 mg	H_2O_2/p-HBZ*	3.2	60 (10 min)	p-hydroxybenzoic acid	73	-	[101]
$Ce_{0.45}Zr_{0.4}O$-$Fe_{0.15}O_{1.925}$	10 mg	5 mL	9	70 (1 h)	Leachate	>50	-	[102]
CeO_2 (CP-2)	0.5	5	2	25 (1 h)	Neutral red	81.27	-	Present work

*PB: Prussian blue; ATP: attapulgite; CP-2: ceria polishing powder; * molar ratio of 14.*

$^{\bullet}OH$ and $HO_2^{\bullet}$ radicals in both liquid and solid phases, HO_2^- and oxygen molecules are formed according to reactions given in Eqs. AS to AU. Even in the absence of extrinsic dopants, a substantial concentration of point defects can exist in ceria as a result of partial reduction of Ce^{4+} to Ce^{3+} (the most stable configuration). Two main point defects may exist, depending on the dopant type and prevalence of oxygen deficiency. Cation defects, Ce^{3+} (in oxygen-deficient ceria) and Do^{3+} (in doped ceria). Every two cation defect centers in the structure are balanced by one oxygen-vacancy defect, V_O [81, 82]. Moreover, the substituted Ce^{4+} by Fe^{3+} in CeO_2, as evidenced by XRD results, caused lattice contraction and formed more oxygen vacancies (V_O). The oxygen vacancies (V_O) react with dissolved oxygen (O_2) and electron (e^-) to generate superoxide radical anions ($^{\bullet}O_2^-$) and singlet oxygen ($^1O_2$, Eq. AV). In another route, further $HO_2^{\bullet}$ radicals are generated through the reaction between produced $^{\bullet}O_2^-$ species and H^+ molecules (Eq. AW). Ultimately, reactive oxygen species (ROS), including $^{\bullet}OH$, as the prominent active species, $^{\bullet}O_2^-$, $^1O_2^{\bullet}$, and, $HO_2^{\bullet}$, as the supporter active groups, might reduce NR dye to intermediates that are mineralized into H_2O and CO_2 [83-85] (Eq. AX). The plausible mechanisms of heterogeneous Fenton-like reaction over α-Fe_2O_3/REO-CP-2/H_2O_2 system can be proposed as follows:

$$Fe^{3+} + H_2O_2 \rightarrow Fe^{2+} + HO_2^{\bullet} + H^+ \quad (AN)$$

$$Fe^{2+} + H_2O_2 \rightarrow Fe^{3+} + {}^{\bullet}OH + OH^- \quad (AO)$$

$$Ce^{4+} + H_2O_2 \rightarrow Ce^{3+} + HO_2^{\bullet} + H^+ \quad (AP)$$

$$Ce^{3+} + H_2O_2 \rightarrow Ce^{4+} + {}^{\bullet}OH + OH^- \quad (AQ)$$

$$Fe^{2+} + Ce^{4+} \rightarrow Fe^{3+} + Ce^{3+} \quad (AR)$$

$$Fe^{2+} + HO_2^{\bullet} \rightarrow Fe^{3+} + HO_2^- \quad (AS)$$

$$Fe^{3+} + HO_2^{\bullet} \rightarrow Fe^{2+} + O_2 + H^+ \quad (AT)$$

$$Ce^{4+} + HO_2^{\bullet} \rightarrow Ce^{3+} + O_2 + H^+ \quad (AU)$$

$$V_O(e^-) + O_2 \rightarrow {}^{\bullet}O_2^-/{}^1O_2 \quad (AV)$$

$$^{\bullet}O_2^- + H^+ \rightarrow HO_2^{\bullet} \quad (AW)$$

$$(^{\bullet}OH, {}^{\bullet}O_2^-, {}^1O_2, HO_2^{\bullet}) + NR \rightarrow \text{Intermediates} \rightarrow CO_2 + H_2O \quad (AX)$$

Comparison of various cerium-based catalysts' performance: the comparison of various cerium-based catalysts' performance for pollutants removal from simulated wastewaters was established. From the structural, morphological, functional surface group, optical properties, and heterogeneous Fenton-like oxidation efficiency point of view, ceria polishing agent (CP-2) could be a promising material for simulated colored wastewater among the cerium-based catalysts reviewed, as displayed in Table XII.

CONCLUSIONS

Cerium oxide polishing powder (CP-2 material) was characterized by XRD, SEM, FTIR, UV-vis DRS, and pH_{PZC} techniques and used as a heterogeneous Fenton-like catalyst for oxidation of neutral red (NR) dye along with hydrogen peroxide (H_2O_2). The effects of various operating parameters such as pH, H_2O_2 concentration, catalyst dosage, dye concentration, temperature, and inorganic salt content were explored. CP-2/H_2O_2 system demonstrated an excellent catalytic efficiency towards the oxidation of NR. Approximately 81.3% of NR degradation was achieved in 60 min with [H_2O_2]=5 mM and initial pH=2 at 25 °C, which was about 1.2 and 7 times higher than that of the pristine CP-2 (67.4%) and H_2O_2 (12.6%), respectively. The decolorization process was thermodynamically feasible, spontaneous, and endothermic. The activation energy (E_a) was 16.4 kJ/mol suggesting that the degradation reaction proceeded with a low energy barrier. The occurrence of the redox Ce^{3+}/Ce^{4+} process on the surface of the CP-2 catalyst could boost the electron transfer of Fe^{3+}/Fe^{2+} to a substantial activation of the heterogeneous Fenton-like systems (Fe- and/or REO-CP-2/H_2O_2). The most reactive oxygen species such as $^{\bullet}OH$, $O_2^{\bullet-}$, $^1O_2$, and $HO_2^{\bullet}$ can reduce effectively NR dye to intermediates that are mineralized into H_2O and CO_2. These results demonstrated that the heterogeneous Fenton-like oxidation process using CP-2 oxide polishing material as a catalyst along with H_2O_2 is a promising technology for the treatment of emerging organic pollutants.

ACKNOWLEDGMENTS

The author gratefully acknowledges the financial support from the Directorate-General for Scientific Research and Technological Development and the Ministry of Higher Education and Scientific Research (Algeria).

REFERENCES

[1] T.B.O. Nunes, N.F. Andrade Neto, L.M.P. Garcia, R.M. Nascimento, M.R.D. Bomio, F.V. Motta, Cerâmica **66**, 378 (2020) 145.
[2] L. Nadjia, E. Abdelkader, B. Naceur, B. Ahmed, J. Rare Earths **36** (2018) 575.
[3] A. Elaziouti, N. Laouedj, A. Bekka, J. King Saud Univ. Sci. **27** (2015) 76.
[4] B. Kakavandi, M. Ahmadi, Ultrason. Sonochem. **56** (2019) 25.
[5] G. Sangami, N. Dharmaraj, Spectrochim. Acta A Mol. Biomol. Spectrosc. **97** (2012) 847.
[6] C. Karunakaran, S.M. Panneerselvam, P. Gomathisankar, Monatsh. Chem. **140** (2009) 1269.
[7] K. Seiji, A. Toshiyuki, J. Mater. Sci. **44** (2009) 2890.
[8] C. Zhong, C. Xueqiang, S. Lixian, Y. He, Adv. Mater.

Res. **239-242** (2011) 998.
[9] C. Karunakaran, R.P. Dhanalakshmi, Gomathisankar, Res. Chem. Intermed. **36** (2010) 361.
[10] J.J. Vora, S.K. Chauhan, K.C. Parmar, S.B. Vasava, S. Sharma, L.S. Bhutadiya, Eur. J. Chem. **6** (2009) 531.
[11] W.S. Chae, J.H. Ko, K.H. Choi, J.S. Jung, Y.R. Kim, J. Anal. Sci. Technol. **1** (2010) 25.
[12] F.A. Frame, E.C. Carroll, D.S. Larsen, M. Sarahan, N.D. Browningb, F.E. Osterloh, Chem. Commun. **0** (2008) 2206.
[13] B. Kakavandi, A.A. Babaei, RSC Adv. **6** (2016) 84999.
[14] M.L. Rache, A.R. Garcia, H.R. Zea, A.M.T. Silva, L.M. Madeira, J.H. Ramirez, Appl. Catal. B **146** (2014) 192.
[15] M.-H. Zhang, H. Dong, L. Zhao, D.-X. Wang, E. Meng, Sci. Total Environ. **670** (2019) 110.
[16] Y. Zhu, R. Zhu, Y. Xi, J. Zhu, G. Zhu, H. He, Appl. Catal. B **255** (2019) 117739.
[17] A. Elaziouti, N. Laouedj, N. Benhadria, Res. J. Chem. Environ. **25** (2021) 52.
[18] N.H. Phu, T.T.K. Hoa, T.N. Van, H.V. Thang, H.P. Le, Appl. Catal. B **34** (2001) 267.
[19] K. Parida, A.C. Pradhan, Ind. Eng. Chem. Res. **49** (2010) 8310.
[20] S. Karthikeyan, C.J. Magthalin, A.B. Mandal, G. Sekaran, RSC Adv. **4** (2014) 19183.
[21] I. Ursachi, A. Stancu, A. Vasile, J. Colloid Interf. Sci. **377** (2012) 184.
[22] P. Shukla, S. Wang, H. Sun, H.M. Ang, M. Tadé, Chem. Eng. J. **164** (2010) 255.
[23] M.P. Pachamuthu, S. Karthikeyan, G. Sekaran, R. Maheswari, A. Ramanathan, Clean (Weinh) **43** (2015) 375.
[24] M. Idrissi, Y. Miyah, Y. Benjelloun, M. Chaouch, J. Mater. Environ. Sci. **7** (2016) 50.
[25] W. Wang, Q. Zhu, F. Qin, Q. Dai, X. Wang, Chem. Eng. J. **33** (2018) 226.
[26] M. Dükkanci, G. Gündüz, S. Yilmaz, R. Prihod'ko, J. Hazard. Mater. **181** (2010) 343.
[27] L. Parimala, J. Santhanalakshmi, React. Kinet. Mech. Catal. **109** (2013) 393.
[28] D. Xu, F. Cheng, Q. Lu, P. Dai, Ind. Eng. Chem. Res. **53** (2014) 2625.
[29] R. Doong, S. Chang, C. Tsai, Appl. Catal. B **129** (2013) 48.
[30] X. Zhang, Y. Ding, H. Tang, X. Han, L. Zhu, N. Wang, Chem. Eng. J. **236** (2014) 251.
[31] F.L. Lam, A.C. Yip, X. Hu, Ind. Eng. Chem. Res. **46** (2007) 3328.
[32] M.P. Pachamuthu, V.V. Srinivasan, R. Maheswari, K. Shanthi, A. Ramanathan, Catal. Sci. Technol. **3** (2013) 3335.
[33] J.L. Zhan, A. Ghafar, J.K. Hyun, H.Y. Seong, O.C. Sung, Nanoscale Res. Letr. **9** (2014) 1.
[34] L.J. Xu, J.L. Wang, Appl. Catal. B **123** (2012) 117.
[35] W. Luo, L.H. Zhu, N. Wang, H.Q. Tang, M.J. Cao, Y.B. She, Environ. Sci. Technol. **44** (2010) 1786.
[36] X. Yang, P.F. Tian, C. Zhang, J. Xu, J. Gong, Y.F. Han, Appl. Catal. B **134-135** (2013) 145.
[37] F. Ji, C.L. Li, J.H. Zhang, L. Deng, Desalination **269** (2011) 284.
[38] S. Fukuchi, R. Nishimoto, M. Fukushima, Q. Zhu, Appl. Catal. B **147** (2014) 411.
[39] A.L.T. Pham, F.M. Doyle, D.L. Sedlaka, Water Res. **46** (2012) 6454.
[40] C. Han, Z. Lizhong, Z. Hehua, Y. Dongju, Z. Qian, Z. Xiufeng, L. Jianhui, J. Mol. Catal. A Chem. **406** (2015) 72.
[41] M. Punzi, B. Mattiasson, M. Jonstrup, J. Photochem. Photobiol. A **248** (2012) 30.
[42] F. Mendez-Arriaga, S. Esplugas, J. Gimenez, Water Res. **44** (2010) 589.
[43] R. Gonzalez-Olmos, M.J. Martin, A. Georgi, F.-D. Kopinke, I. Oller, S. Malato, Appl. Catal. B **125** (2012) 51.
[44] B.M. Zimmermann, S. Silvestri, J. Leichtweis, G.L. Dotto, E.S. Mallmann, E.L. Foletto, Cerâmica **65**, 373 (2019) 147.
[45] V.M. Figueiredo, J.B. Lourenço, N.J.S. de Vasconcellos, W.L. da Silva, Cerâmica **66**, 380 (2020) 367.
[46] S.L.A. Dantas, Y.F. Gomes, A.L. Lopes-Moriyama, M.A. Correa, C.P. Souza, Cerâmica **66**, 380 (2020) 460.
[47] G.C.S. Shekar, K. Alkanad, A. Hezam, A. Alsalme, N. Al-Zaqri, N.K. Lokanath, J. Mol. Liq. **335** (2021) 116.
[48] R. Fiorenza, S.A. Balsamo, L. D'Urso, S. Sciré, M.V. Brundo, R. Pecoraro, E.M. Scalisi, V. Privitera, G. Impellizzeri, Catalysts **10** (2020) 446.
[49] L.J. Xua, J.L. Wang, Appl. Catal. B **142** (2013) 396.
[50] L. Soler, A. Casanovas, A. Urrich, I. Angurell, J. Llorca, Appl. Catal. B **197** (2016) 47.
[51] S.B. Hammouda, F.P. Zhao, Z. Safaei, I. Babu, D.L. Ramasamy, M. Sillanpää, Appl. Catal. B **218** (2017) 119.
[52] P. Gao, X.J. Chen, M.J. Hao, F. Xiao, S.X. Yang, Chemosphere **228** (2019) 521.
[53] N.Q. Zhang, J.Y. Chen, Z.Q. Fang, E.P. Tsang, Chem. Eng. J. **369** (2019) 588.
[54] J. Zhu, G. Zhang, G. Xian, N. Zhang J. Li, Front. Chem. **7** (2019) 796.
[55] Y. Zhang, R. Xiao, S. Wanga, H. Zhu, H. Song, G. Chen, H. Lin, J. Zhang, J. Xiong, J. Hazard. Mater. **398** (2020) 122863.
[56] E.A. Moawed, Y. Alqarni, SAMPRE **3** (2013) 18.
[57] A.A.A. Zuki, M. Awang, A. Asmadi, M. Awang, M.H. Zain, Int. J. Appl. Chem. **12** (2016) 29.
[58] B.D. Cullity, *Elements of X-ray diffraction*, Addison-Wesley Publ. (1956) 98.
[59] ISO 9277, "Determination of the specific surface area of solids by gas adsorption using the BET method" (2010).
[60] M.P. Gómez-Tena, J. Gilabert, J. Toledo, E. Zumaquero, C. Machí, in Qualicer **14**, Castellón (2013).
[61] S. Ahadi, N.S. Moalej, S. Sheibani, Solid State Sci. **96** (2019) 105975.
[62] T.N. Ravishankar, T. Ramakrishnappa, G. Nagaraju, H. Rajanaika, Chem. Open **4** (2015) 146.
[63] A.M. Abdulkarem, J. Li, A.A. Aref, L. Ren, E.M. Elssfah, H. Wang, Y. Ge, Y. Yu, Mater. Res. Bull. **46** (2011) 1443.
[64] F. Cheviré, F. Munoz, C.F. Baker, F. Tessier, O. Larcher, S. Boujday, C. Colbeau-Justin, R.J. Marchand, Solid State

Chem. **179** (2006) 3184.
[65] A. Elaziouti, N. Laouedj, A. Bekka, R.N. Vannie, Sci. Technol. A **39** (2014) 9.
[66] Y. Xu, M.A.A. Schoonen, Am. Mineral. **85** (2000) 543.
[67] S. Phanichphant, A. Nakaruk, D. Channei, Appl. Surf. Sci. **387** (2016) 214.
[68] D.E. Yates, S. Levine, T.W. Healy, J. Chem. Soc. Faraday Trans. **70** (1974) 1807.
[69] N. Wang, J. Chen, Q. Zhao, H. Xu, RSC Adv. **7** (2017) 52524.
[70] N. Benhadria, A. Elaziouti¸ N. Laouedj, M. Sellami, N. Bettahar, Mater. Res. Bull. **4** (2016) 491.
[71] H. Lin, H. Zhang, X. Wang, L.G. Wang, J. Wu, Sep. Purif. Technol. **122** (2014) 533.
[72] M. Dogan, M. Alkan, A. Turkyilmaz, Y. Ozdemir, J. Hazard. Mater. **109** (2004) 141.
[73] B. Pare, P. Singh, S.B. Jonnalagadda, Indian J. Chem. Technol. **17** (2010) 391.
[74] M. Neamtu, C. Catrinescu, A. Kettrup, Appl. Catal. B **51** (2004) 149.
[75] Y. Wang, R. Priambodo, H. Zhang, Y.H. Huang, RSC Adv. **5** (2015) 45276.
[76] A.A. Giwa, I.A. Bello, A.B. Olabintan, O.S. Bello, T.A. Saleh, Heliyon **6** (2020) e04454
[77] J. He, Y. Zhang, Y. Guoa, G. Rhodesa, J. Yeom, H. Li, W. Zhang, Environ. Int. **132** (2019) 105105.
[78] S. Zhao, C. Wang, D. Wang, Y. Wang, F. Liu, RSC Adv. **6** (2016) 18800.
[79] N. Wang, J. Chen, Q. Zhao, H. Xu, RSC Adv. **7** (2017) 52524.
[80] E.G. Heckert, S. Seal, W.T. Self, Environ. Sci. Technol. **42** (2008) 5014.
[81] M. Noorisepehr, B. Kakavandi, A.A. Isari, F. Ghanbari, E. Dehghanifard, Sep. Purif. Technol. **250** (2020) 116950.
[82] S.S. Rezaei, B. Kakavandi, M. Noorisepehr, A.A. Isari, S. Zabih, Sep. Purif. Technol. **258** (2021) 117936.
[83] R.L. Schmitt, A. Nenning, O. Kraynis, R. Korobko, A.I. Frenkel, I. Lubomirsky, S.M. Hailef, J.L.M. Rupp, Chem. Soc. Rev. **49** (2020) 554.
[84] M. Asnavandi, Y. Yin, Y. Li, C. Sun, C. Zhao, ACS Energy Lett. **3** (2018) 1515.
[85] S. Hussain, E. Aneggi, D. Goi, Environ. Chem. Lett. **19** (2021) 2405.
[86] S.B. Hammouda, F. Zhao, Z. Safaei, I. Babu, D.L. Ramasamy, M. Sillanpaa, Appl. Catal. B **218** (2017) 119.
[87] H. Xie, J. Zeng, G. Zhou, Environ. Sci. Pollut. Res. **27** (2020) 846.
[88] L. Xu, J. Wang, Sep. Purif. Technol. **149** (2015) 255.
[89] F. Chen, X. Shen, Y. Wang, J. Zhang, Appl. Catal. B **121** (2012) 223.
[90] N. Zhang, Y. Yi, J. Lian, Z. Fang, Chem. Eng. J. **395** (2020) 124897.
[91] P. Ji, L. Wang, F. Chen, J. Zhang, Chem. Cat. Chem. **2** (2010) 1552.
[92] N. Zhang, J. Chen, Z. Fang, E.P. Tsang, Chem. Eng. J. **369** (2019) 588.
[93] N. Zhang, E.P. Tsang, J. Chen, Z. Fang, D. Zhao, J. Colloid Interface Sci. **558** (2020) 163.
[94] H. Hamoud, G. Finqueneise, B. Azambre, J. Environ. Manage. **195** (2017) 195.
[95] Y. Zhang, R. Xiao, S. Wang, H. Zhu, H. Song, G. Chen, H. Lin, J. Zhang, J. Xiong, J. Hazard. Mater. **398** (2020) 122863.
[96] G. Guoqiang, Z. Pan, Z. Xiaoqing, L. Juan, L. Jingjing, Z. Conglu, H. Xiaohong, J. Alloys Compd. **725** (2017) 472.
[97] G. Guoqiang, L. Juan, Z. Zhixi, Y. Ziran, Z. Conglu, H. Xiaohong, Chemosphere **168** (2017) 254.
[98] S. Chong, G. Zhang, N. Zhang, Y. Liu, T. Huang, H. Chang, J. Hazard. Mater. **334** (2017) 150.
[99] T. Zhang, L. Dong, J. Du, C. Qian Y. Wang, RSC Adv. **10** (2020) 23431.
[100] G. Xian, N. Zhang, G. Zhang, Y. Zhang Z. Zou, Water Sci. Technol. **79** (2019) 1675.
[101] T. Hammedi, M. Triki, M.G. Alvarez, J. Llorca, A. Ghorbel, Z. Ksibi, F. Medina, Water Sci. Technol. **79** (2019) 1276.
[102] E. Aneggi, V. Cabbai, A. Trovarelli, D. Goi, Int. J. Photoenergy **2012** (2012) 694721.

(Rec. 01/08/2021, Rev. 01/10/2021, 21/11/2021, Ac. 30/12/2021)

(cc) BY-NC